REPORT DOCUMENTATION PAGE

Form Approved
OMB No. 0704-0188

Public reporting burden for this collection of information is estimated to average 1 hour per response, including the time for reviewing instructions, searching existing data sources, gathering and maintaining the data needed, and completing and reviewing this collection of information. Send comments regarding this burden estimate or any other aspect of this collection of information, including suggestions for reducing this burden to Department of Defense, Washington Headquarters Services, Directorate for Information Operations and Reports (0704-0188), 1215 Jefferson Davis Highway, Suite 1204, Arlington, VA 22202-4302. Respondents should be aware that notwithstanding any other provision of law, no person shall be subject to any penalty for failing to comply with a collection of information if it does not display a currently valid OMB control number. **PLEASE DO NOT RETURN YOUR FORM TO THE ABOVE ADDRESS.**

1. REPORT DATE *(DD-MM-YYYY)*	**2. REPORT TYPE**	**3. DATES COVERED** *(From - To)*
	Journal Article	

4. TITLE AND SUBTITLE
Classical dynamics of state-resolved hyperthermal O(3P) + H2O(1A1) (Pre-Print)

5a. CONTRACT NUMBER
W9113M-10-C-0082

5b. GRANT NUMBER

5c. PROGRAM ELEMENT NUMBER

6. AUTHOR(S)
Matthew Braunstein and Patrick F. Conforti

5d. PROJECT NUMBER

5e. TASK NUMBER

5f. WORK UNIT NUMBER
Q0PY

7. PERFORMING ORGANIZATION NAME(S) AND ADDRESS(ES)

Spectral Sciences Inc.
4 Fourth Avenue
Burlington, MA 01803

8. PERFORMING ORGANIZATION REPORT NO.

9. SPONSORING / MONITORING AGENCY NAME(S) AND ADDRESS(ES)

Air Force Research Laboratory (AFMC)
AFRL/RQRS
1 Ara Drive
Edwards AFB CA 93524-7013

10. SPONSOR/MONITOR'S ACRONYM(S)

11. SPONSOR/MONITOR'S REPORT NUMBER(S)
AFRL-RQ-ED-JA-2012-291

12. DISTRIBUTION / AVAILABILITY STATEMENT
Approved for public release; distribution unlimited

13. SUPPLEMENTARY NOTES
To be published in Journal of Chemical Physics; Vol 138, Issue 7; Feb 2013
PA Case Number: 12840; Clearance Date: 17 Oct 2012.

14. ABSTRACT
Classical dynamics calculations are performed for O(3P) + H2O(1A1) collisions from 2 to 10 km s-1 (4.1 to 101.3 kcal mol-1), focusing on product internal energies. Several methods are used to produce ro-vibrationally state-resolved product cross sections and to enforce zero-point maintenance from analysis of the classical trajectories. Two potential energy surfaces are used: 1) a recently developed set of global reactive surfaces for the three lowest triplet states which model OH formation, H elimination to make H + OOH, O-atom exchange, and collisional excitation, and 2) a non-reactive surface used in past classical and quantum collision studies. Comparisons to these previous studies suggest that for H2O vibrational excitation, classical dynamics which include Gaussian binning procedures and/or selected zero-point maintenance algorithms can produce results which approximate quantum scattering cross sections fairly well. Without these procedures, the classical cross sections can be many orders of magnitude greater than the quantum cross sections for exciting the bending vibration of H2O, especially near threshold. The classical cross section over-estimate is due to energy borrowing from stretching modes which dip below zero-point values. For results on the reactive surfaces, the present calculations show that at higher velocities there is an unusually large amount of product internal excitation. For OOH, where 40% of available collision energy goes into internal motion, the excited product vibrational and rotational energy distributions are relatively flat and values of the OOH rotational angular momentum exceed J=100. Other product channel distributions show an exponential fall-off with energy consistent with an energy gap law. The present detailed distributions and cross sections can serve as a guide for future hyperthermal measurements of this system.

15. SUBJECT TERMS

16. SECURITY CLASSIFICATION OF:			**17. LIMITATION OF ABSTRACT**	**18. NUMBER OF PAGES**	**19a. NAME OF RESPONSIBLE PERSON**
					Marty Venner
a. REPORT	**b. ABSTRACT**	**c. THIS PAGE**	SAR	45	**19b. TELEPHONE NO** *(include area code)*
Unclassified	**Unclassified**	**Unclassified**			661 275-5091

Classical dynamics of state-resolved hyperthermal $O(^3P) + H_2O(^1A_1)$ collisions

Matthew Braunstein and Patrick F. Conforti

Spectral Sciences Incorporated

4 Fourth Avenue

Burlington, MA 01803

Email: matthew.braunstein@spectral.com

ABSTRACT

Classical dynamics calculations are performed for $O(^3P) + H_2O(^1A_1)$ collisions from 2 to 10 km s^{-1} (4.1 to 101.3 kcal mol^{-1}), focusing on product internal energies. Several methods are used to produce ro-vibrationally state-resolved product cross sections and to enforce zero-point maintenance from analysis of the classical trajectories. Two potential energy surfaces are used: 1) a recently developed set of global reactive surfaces for the three lowest triplet states which model OH formation, H elimination to make H + OOH, O-atom exchange, and collisional excitation, and 2) a non-reactive surface used in past classical and quantum collision studies. Comparisons to these previous studies suggest that for H_2O vibrational excitation, classical dynamics which include Gaussian binning procedures and/or selected zero-point maintenance algorithms can produce results which approximate quantum scattering cross sections fairly well. Without these procedures, the classical cross sections can be many orders of magnitude greater than the quantum cross sections for exciting the bending vibration of H_2O, especially near threshold. The classical cross section over-estimate is due to energy borrowing from stretching modes which dip below zero-point values. For results on the reactive surfaces, the present calculations show that at higher velocities there is an unusually large amount of product internal excitation. For OOH, where 40% of available collision energy goes into internal motion, the excited product vibrational and rotational energy distributions are relatively flat and values of the OOH rotational angular momentum exceed J=100. Other product channel distributions show an exponential fall-off with energy consistent with an energy gap law. The present detailed distributions and cross sections can serve as a guide for future hyperthermal measurements of this system.

Distribution A: Approved for public release; distribution unlimited.

I. INTRODUCTION

Collisions of $O(^3P)$ atom with $H_2O(^1A_1)$ have recently been investigated using hyperthermal crossed beams[1] in the energy range ~50- 80 kcal mol^{-1} (~7-9 km s^{-1}). At these energies, several reactions occur:

(1) OH formation: $O(^3P) + H_2O(X,^1A_1) \rightarrow OH(X,^2\Pi) + OH(X,^2\Pi)$, $\Delta H_0 = 15.8$ kcal mol^{-1},[2], $\Delta E^{\dagger}$~18 kcal mol^{-1} [3]

(2) H-elimination: $O(^3P) + H_2O(X^1A_1) \rightarrow OOH(X,^2A'') + H(X^2S)$ $\Delta H_0 = 53.4$ kcal mol^{-1} [4], $\Delta E^{\dagger}$ ~60 kcal mol^{-1} [3]

(3) O-atom exchange: $O(^3P) + H_2O'(X,^1A_1) \rightarrow O'(^3P) + H_2O(X,^1A_1)$, $\Delta H_0 = 0.0$ kcal mol^{-1}, $\Delta E^{\dagger}$ ~33 kcal mol^{-1} [5]

In addition, non-reactive collisional excitation occurs:

(4) Collisional excitation: $O(^3P) + H_2O(X,^1A_1, (\nu_1\nu_2\nu_3,JK_aK_c)) \rightarrow O(^3P) + H_2O(X,^1A_1(\nu_1'\nu_2'\nu_3',J'K_a'K_c'))$

In Eqs. (1-3), the $\Delta E^{\dagger}$ values are approximate threshold energies based on the surfaces of Ref. (3) and include zero-point energy.

Studies of $O(^3P) + H_2O(^1A_1)$ hyperthermal collisions go back nearly 40 years to measurements of infrared radiation in shock tubes.[6] In the 1980's, cross sections for vibrational excitation were calculated using quasi-classical trajectory (QCT) methods[7] on a global non-reactive potential surface[8]. These cross sections were in fair agreement with the limited experimental data available. Slightly later, approximate quantum scattering calculations with the same surface were performed.[9] The QCT and approximate quantum cross sections were orders of magnitude apart, even at relatively large collision velocities. These differences have made it difficult to interpret the measurements. They also present a large puzzle in assessing the accuracy of classical versus quantum methods.

We note that recently there have been several advances in classical dynamics methods for determining state-resolved excitation and reaction cross sections in polyatomic systems. These have led to impressive results for several systems: $CH_4 + Cl \rightarrow HCl + CH_3$,[10] $OH + D_2 \rightarrow HOD + D$,[11] $(H_2O)_2$ and $(D_2O)_2$ dissociation,[12] and rotational excitation of H_2O by H_2.[13] In particular for the reaction, $OH + D_2 \rightarrow HOD + D$, Sierra *et al.*[11] use standard QCT methods, plus two key advances: determination of vibrational quantum numbers through analysis of product momenta and coordinates,[14,15] and a Gaussian binning procedure which weights trajectories where classically determined vibrational quantum numbers are close

Distribution A: Approved for public release; distribution unlimited.

to "allowed" quantum integer values.[16,17] With these procedures, Sierra *et al.*[11] obtained excellent agreement with angle-velocity measurements of product D-atoms, showing distinct vibrational structure of product HOD bending and stretching modes. For $(H_2O)_2$ and $(D_2O)_2$ dissociation, Czako *et al.*[12] use similar binning procedures, except the Gaussian weights are determined by vibrational energies instead of quantum numbers. QCT methods, which reproduce more accurate benchmark quantum scattering results and have been tested against experimental measurements, could be a practical alternative to quantum scattering methods.

The primary purpose of this paper is to present results of $O(^3P) + H_2O(^1A_1)$ QCT calculations using these recently developed classical dynamics methods. The focus is on product internal energies and ro-vibrational, state-specific cross sections for Eqs. (1-4). Particular attention is given to vibrational excitation in Eq. 4 to better understand previous hyperthermal measurements and modeling. In one set of QCT calculations, the work of Refs. 7 and 9 is re-examined. In this previous work, conventional histogram binning QCT[7] and approximate quantum scattering[9] calculations for vibrational excitation, Eq. (4), were performed using the non-reactive $O(^3P) + H_2O(^1A_1)$ surface of Refs. 7,8, and 18. We wish to understand the more than order of magnitude difference in vibrational excitation cross sections from these two studies in light of recent advances in classical dynamics methods. For the first set of QCT calculations reported here, the same non-reactive surface of Ref. 7 was used. Ro-vibrational H_2O excitation cross sections, Eq. 4, were determined with conventional histogram binning and Gaussian binning at collision velocities 2, 4, 6, and 8 km s^{-1} (4.1, 16.2, 36.5, and 64.8 kcal mol^{-1}), with 10^6 trajectories per velocity. For these QCT calculations, a number of different methods were used and compared for analysis of coordinates and momenta to determine product vibrational quantum numbers. A chief finding of these QCT calculations is that Gaussian binning dramatically decreases the vibrational excitation cross section, (Eq. 4), for the H_2O bending mode, compared to conventional histogram binning, especially near threshold. With conventional histogram binning, the bending mode will tend to borrow energy from stretching vibrations which dip below their zero point energy, and the bending excitation cross sections become un-physically large. The Gaussian binned QCT results were in fair agreement with the approximate quantum scattering calculations of Ref. 9 using the same surface. These results indicate that the several orders of magnitude difference between the QCT H_2O bending cross sections of Ref. 7 and the approximate quantum scattering cross sections of Ref. 9 using the same surface are due to quantum effects that can be effectively accounted for with Gaussian binning. For exciting the stretching modes, we were unable to reproduce the QCT cross sections of Ref. 7 with the same QCT histogram binning procedures and other parameters used in that study. The stretching vibrational excitation cross sections we obtained with histogram binning were much smaller in magnitude than those of Ref. 7 and were much more in line with the approximate quantum scattering results of Ref. 9. The stretching

Distribution A: Approved for public release; distribution unlimited.

vibrational excitation cross sections changed little with Gaussian binning. We performed approximately 200 times more trajectories per velocity than Ref. 7, but otherwise used very similar methods to generate the cross sections.

In a second series of calculations, the recently developed $O(^3P) + H_2O(^1A_1)$ surfaces of Ref. 3 were used, including all reactive channels (Eqs. 1-3), for the three lowest triplet electronic states. The surfaces were fits of CASSCF+MP2 electronic structure calculations using a polynomial function of the bond distances, with built-in permutational symmetry of like-atoms.[19] These calculations were performed at velocities of 2, 4, 6, 8, and 10 km s^{-1} (4.1, 16.2, 36.5, 64.8, 101.3 kcal mol^{-1}), and include ~10^5 trajectories per surface per velocity. As with the first set of QCT calculations, Gaussian binning dramatically decreases the non-reactive vibrational excitation cross section, (Eq. 4), for the H_2O bending mode, compared to conventional histogram binning, especially near threshold. In contrast, conventional histogram binning and Gaussian binning gave similar results for the reactive channels, Eqs. (1-3), except very close to threshold. For OOH, where 40% of available collision energy goes into internal motion, the excited product vibrational and rotational energy distributions are relatively flat, and values of the rotational angular momentum can reach values greater than J=100. Other product channel distributions show an exponential fall-off with energy consistent with an energy gap law. We also compare these results to the first set of QCT calculations using the surfaces of Refs. 7, 8, and 18 to examine the sensitivity of the cross sections to the potential used. For excitation of the bending mode, there is good agreement between the two QCT Gaussian binning results, except very close to threshold. For stretching excitation, both surfaces give small cross sections, but there are significant differences. This is mainly due to the reactive nature of the Ref. 3 surfaces which break/form bonds as the O-H bonds change. For the two sets of QCT calculations reported here, the experimental results of Ref. 6 fall well outside the quoted experimental uncertainty and statistical uncertainty of the present calculations. As a further test of the quality of the potential surfaces, we also performed QCT rate constant calculations at fixed temperatures for OH formation, Eq. (1) and the reverse of Eq. (1), where there is a great deal of measured data.[20-23] For these rate constants, the present results agreed well with measurements.

Since $H_2O(^1A_1)$ zero-point energy (~12.9 kcal mol^{-1})[24] can be a significant fraction of the collision energy, especially at the lower collision velocities studied, we also implemented procedures to maintain zero-point energy during the classical trajectory, following the work of Refs. 25 and 26. Zero-point maintenance in QCT calculations may be important in certain kinds of reactions, especially involving collision complexes with long lifetimes. However, the implementation of zero-point maintenance has to be performed with great care. For the $O + H_2O$ collisions studied here, in many instances, we found that it is difficult to cleanly separate vibrational and rotational type motion during the

Distribution A: Approved for public release; distribution unlimited.

collision. When the O and H_2O reactants were close together, this sometimes resulted in 'low frequency vibrational modes' being used to help maintain zero-point vibrational energy, and a leaking of what may be rotational energy into vibration. As a result, energetically closed vibrational excitation channels (channels not energetically allowed quantum mechanically) close to threshold began to pick up significant probability. When we restricted the zero-point maintenance procedures to portions of the trajectory where the reactants and products were well-separated and there was better separation of rotational and vibrational motion, the results closely matched the Gaussian binning results. Our conclusion is that the zero-point maintenance procedures when applied to separate product and reactant portions of the trajectory were attempting to enforce the same kind of partitioning of energy among the vibrational modes that result from Gaussian binning procedures for the processes studied here.

The paper proceeds as follows. Section II describes details of the QCT calculations, including the methods for analysis of products for assignment of polyatomic ro-vibrational quantum numbers. Section II also describes procedures used in Gaussian binning and zero-point maintenance, which are both closely related to determination of the polyatomic quantum numbers. Section III presents results of QCT calculations on the non-reactive surface of Refs. 8 and 18, focusing on vibrational excitation. Results are compared to the QCT calculations of Ref. 7 and the approximate quantum scattering calculations of Ref. 9. Section IV presents results of QCT calculations using the recently developed $O(^3P) + H_2O(^1A_1)$ surfaces of Ref. 3, focusing on the internal product energies of processes in Eqs. (1-4). Section V gives conclusions.

II. METHODS

A. POTENTIAL SURFACES

Two different potential energy surfaces were used for the $O(^3P) + H_2O(^1A_1)$ dynamics calculations. One was the non-reactive $O(^3P) + H_2O(^1A_1)$ surface developed by Bartlett, Redmon, Schatz, and Garrett (BRSG).[7,8,18] This surface is a Sorbie-Murrell many-body fit of *ab initio* MBPT calculations,[27] including an analytical fit to the non-bonding, pair-wise and three body interactions between O and each atom in the H_2O molecule as well as an analytical fit to the *ab initio* surface of H_2O. The authors of the BRSG surface note that it is best suited to collision energies up to 3.0 eV (69.2 kcal mol^{-1}).[7] As discussed in the previous section, the BRSG surface was previously used for quasi-classical trajectory calculations[8] and quantum scattering calculations.[9] While there have been some modifications to the BRSG surface by Schwenke for QCT studies,[28] the present work uses the original BRSG surface to enable a more direct comparison of results with Refs. 7 and 9.

Distribution A: Approved for public release; distribution unlimited.

The second $O(^3P) + H_2O(^1A_1)$ potential was recently developed by Conforti, Braunstein, Braams, and Bowman (CBBB).[3] The global CBBB surface is actually a set of the three lowest triplet electronic states for the $O(^3P) + H_2O(^1A_1)$ system. Approximately 10^5 *ab initio* single point energies were calculated using CASSCF+MP2 theory, which sampled geometries including reactive (Eqs. 1-3) and non-reactive (Eq. 4) collisions. In addition, many configurations were included for high-energy, short bond distance interactions in order for the resulting potential energy surface to be applicable at high collision velocities. For the fit, basis functions of the six inter-nuclear bond distances yielded approximately 500 terms for each electronic surface. The fitting procedure is described in great detail in Ref. 19. The CBBB surfaces are best suited for collision energies up to approximately 150 kcal mol^{-1}.

Since we wish to understand the sensitivity of the dynamics simulations to the potential surfaces used, it is appropriate to examine differences between the BRSG and CBBB surfaces. In Figure 1, contour plots are shown of the $O + H_2O$ system using the BRSG (Figure 1a and 1c) and CBBB surfaces (Figure 1b and 1d). For Figure 1a and 1b, the H_2O molecule is close to the equilibrium geometry, and the O-O bond distance is varied within H_2O plane. For Figure 1c and 1d, the H_2O molecule is such that one of the O-H bonds is stretched from its equilibrium value, and the O-O bond distance is varied in the H_2O plane. For the CBBB surface in Figure 1d, the lower energy region indicates the formation of an OH bond. The corresponding BSRG geometries in Figure1c show a deep well on each side of the H-atom that has been stretched. The BRSG and CBBB surfaces in Figure 1a and Figure 1b very closely resemble each other. However, the surfaces are clearly different in Figure 1c and 1d. We note that the BRSG surface is not intended to be reactive. But 8 km s^{-1} (64.8 kcal mol^{-1}) collisions should access these geometries, and so the resulting dynamics may be significantly different.

B. Classical dynamics formulation

In this section we review several procedures, recently developed by others and used in the present work for computing QCT state-resolved cross sections for polyatomics. We start with methods for separating rotational and vibrational motion in polyatomic molecules. This separation leads to algorithms for determining vibrational quantum numbers and to approaches for maintaining zero-point energy in classical dynamics calculations. Finally, we review Gaussian binning procedures for determining state-resolved cross sections.

1. Separation of rotational and vibrational motion

Although methods for determining vibrational quantum numbers for diatomic products in QCT calculations are well-defined,[29] corresponding procedures for polyatomic molecules are less well-known.

Distribution A: Approved for public release; distribution unlimited.

This is mainly due to the fact that polyatomic products require an extra step of separating rotational and vibrational motion. Several authors[14,15] have discussed procedures for this separation. In the present work, we follow the approach of Rhee and Kim,[30] a general formulation which leads straightforwardly to algorithms for zero-point maintenance and to several alternate determinations of vibrational quantum numbers.

The Rhee and Kim approach (Ref. 30) starts by defining mass scaled Cartesian coordinates for a system of *N* atoms in the center of mass frame with the center of mass velocity removed. We denote the atomic coordinates:

$$\bar{x} \ni \{x_\alpha^i \sqrt{m_\alpha}, \alpha = 1,2, \dots, N, i = x, y, z\}. \tag{5}$$

where m_α is the atomic mass of atom α. For convenience, vector notation is used. Therefore the symbol, $\bar{x}$, denotes a vector of three Cartesian, space fixed coordinates for each of the atoms, α. We define the angular velocity, $\bar{\omega}$, in the usual way:

$$\bar{\omega} = \overline{\overline{I^{-1}}} \sum_\alpha^N \bar{x}_\alpha \times \bar{x}'_\alpha \tag{6}$$

where the inertia tensor, $\bar{\bar{I}}$, is defined as:

$$\bar{\bar{I}} = \sum_\alpha^N [1\ (\bar{x}_\alpha \cdot \bar{x}_\alpha) - \cdot\, \bar{x}_\alpha \bar{x}_\alpha \cdot] \,. \tag{7}$$

The separation of vibrational and rotational motion following Rhee and Kim[30] starts by writing the Cartesian velocity in terms of pure vibrational and rotational components that can be separated:

$$\dot{\bar{x}}_\alpha = \bar{v}_\alpha + \bar{u}_\alpha + \bar{\omega}_r \times \bar{x}_\alpha. \tag{8}$$

where the sum, $\bar{v}_\alpha + \bar{u}_\alpha$, is the pure vibrational component and $\bar{\omega}_r \times \bar{x}_\alpha$ is the pure rotational component. The vector, $\bar{u}_\alpha$, is defined:

$$\bar{u}_\alpha = (\bar{\omega} - \bar{\omega}_{r)} \times \bar{x}_\alpha. \tag{9}$$

The vector, $\bar{\omega}_r$, is defined in terms of the dynamic equilibrium vectors, $\bar{a}_\alpha$,

$$\bar{\omega}_r = \overline{\overline{I'^{-1}}} \cdot \sum_\alpha^N \bar{a}_\alpha \times \dot{\bar{x}}_\alpha \tag{10}$$

where,

$$\bar{\bar{I}}' = \sum_\alpha^N [1\ (\bar{x}_\alpha \cdot \bar{a}_\alpha) - \cdot\, \bar{x}_\alpha \bar{a}_\alpha \cdot] \,. \tag{11}$$

The dynamic equilibrium vectors are extremely important to the formulation. As we shall see, the dynamic equilibrium vectors are determined by applying a rotation to the molecule's static equilibrium

Distribution A: Approved for public release; distribution unlimited.

vectors so that they align with the present position in the trajectory of the rotating molecule. Defining the vibrational displacement vector, $\bar{\xi}_\alpha$,

$$\bar{\xi}_\alpha = \bar{x}_\alpha - \bar{a}_\alpha, \tag{12}$$

the so-called Eckart condition (Ref. 31), which is really a restatement of angular momentum conservation, is:

$$\sum_\alpha^N \bar{a}_\alpha \times \bar{\xi}_\alpha = \bar{0}. \tag{13}$$

The dynamic equilibrium vectors, $\bar{a}_\alpha$, are found by the Eckart transform,

$$\bar{a}_\alpha = \bar{\bar{F}}\bar{c}_\alpha, \tag{14}$$

where $\bar{\bar{F}}$ is a matrix which transforms the fixed molecular equilibrium Cartesian positions, $\bar{c}_\alpha$, to the dynamic equilibrium positions, $\bar{a}_\alpha$. The Eckart transform[31] in the above equation essentially rotates the molecular equilibrium to align with the present position of the molecule, so that any displacements are purely vibrational. Thus the vibrational motion is cleanly isolated. Once $\bar{\omega}_r$ is found, the vectors $\bar{v}_\alpha$ and $\bar{u}_\alpha$ can then be solved for in terms of known vector quantities using the above equations.

2. Determination of quantum numbers

Now that the vibrational motion of the polyatomic has been isolated in the vectors $\bar{v}_\alpha + \bar{u}_\alpha$, the next step is to separate the vibrational motion into specific modes and to determine energies and semi-classical quantum numbers of these modes. This is done by diagonalizing the mass-weighted second derivative of the potential matrix (Hessian) at each time-step. The eigenvectors, $\bar{\bar{L}}_l$, are used to determine the momentum ($\dot{Q}$) and position (Q) of each vibrational mode, indexed by *l*:

$$\dot{Q}_l = \bar{\bar{L}}_l \cdot (\bar{v} + \bar{u}), \tag{15}$$

$$Q_l = \bar{\bar{L}}_l \cdot \bar{\xi}. \tag{16}$$

There are several approximate ways the vibrational potential energy of a particular mode can be defined. In the harmonic approximation (HA),[30] the mode potential energy is:

$$V_{vib,l} \approx \frac{1}{2}\lambda_l^2 \dot{Q}_l^2. \tag{17}$$

In the elimination method (EM),[30] the mode potential energy is:

$$V_{vib,l} \approx V\left(\overline{a + Q_l \bar{\bar{L}}_l}\right) - V(\bar{a}). \tag{18}$$

For both methods the normal mode kinetic energy is:

Distribution A: Approved for public release; distribution unlimited.

$$T_{vib,l} = \frac{1}{2}\dot{Q}_l^2. \quad (19)$$

The total vibrational energy of a particular mode is:

$$E_{vib,l} = T_{vib,l} + V_{vib,l}. \quad (20)$$

The quantum number of a particular mode is then defined as:

$$N_{vib,l} = int(\frac{E_{vib,l}}{E_{mode}}), \quad (21)$$

where E_{mode} is the harmonic energy of that mode, and *int* stands for integer. In practice, we estimate the vibrational mode energy by averaging the energy of the collided product over several vibrational periods, and then we assign quantum numbers for a particular trajectory based on this average. During the averaging, the summed mode energies would sometimes differ greatly from the total vibrational energy, mainly due to geometries where the approximate mode potential energies were poor. We therefore used a cutoff energy of 10 kcal mol^{-1}. If the summed mode energies and total energies differed by more than this cutoff, then the analysis point was not included in the average.

Schatz and coworkers use a different method to compute quantum numbers from the classical eigenmode momentum and position.[15] They determine the classical action integral involving the momentum and position of a particular mode over several vibrational periods and then relate this to a quantum number following the WKB method. This is done with an FFT method. In our work, we also compute quantum numbers with this procedure, denoted as "ACT" cross sections. We have found all methods (HA, EM, and ACT) in general give similar results.

3. Zero-point maintenance

In our work, we have also employed algorithms to maintain zero-point energy during and after collisions following the work of several groups.[14,25,26] These algorithms also start with the separation of rotational and vibrational motion. We start by defining the momentum vector for the system which is the time derivative of the mass scaled Cartesian coordinates:

$$\bar{p} = \dot{\bar{x}}. \quad (22)$$

We then generate the projected Hessian matrix as discussed in Bonhommeau and Truhlar (Eqs. 7 and 8).[26] This is done by taking the second derivative potential matrix (Hessian), creating a projection operator, and then using the operator to project out the translation and rotation from the Hessian to isolate the vibrational motion. We then calculate the eigen-frequencies and eigenvectors of the projected Hessian. The eigen-frequencies are labeled, Ω_l, and the eigenvectors are labeled,

Distribution A: Approved for public release; distribution unlimited.

$\bar{\bar{L}}_l^{proj}$, for the *l*-th vibrational component. We proceed by defining the normal mode momenta, P, for all the real, non-zero vibrational modes, *l*.

$$P_l = \bar{\bar{L}}_l^{proj} \cdot \bar{p}. \tag{23}$$

In practice, we impose a lower energy limit of 50 cm^{-1} to a vibrational mode. Therefore, we only treat the, *3N-q*, (q≥6), modes above this lower limit. The instantaneous energy of mode *l* is defined as:

$$E_l = 0.5\left[P_l^2 + \left(\frac{D_l}{\Omega_l}\right)^2\right]. \tag{24}$$

where the D_l are projected mass-scaled, first derivatives of the potential:

$$D_l = \bar{\bar{L}}_l^{proj} \cdot \overline{\nabla V}, \tag{25}$$

where in vector notation:

$$\overline{\nabla V} \ni \{\frac{\nabla V_\alpha^i}{\sqrt{m_\alpha}}, \alpha = 1.2 \ldots., N, i = x, y, z\}. \tag{26}$$

We now define the local vibrational mode energy, in atomic units, as:

$$E_{zpe,l} = 0.5\,\Omega_l\,. \tag{27}$$

We use the following "mTRAPZ" criterion[26] for when to enforce zero-point maintenance:

$$\sum_{l=1}^{3N-q} E_l \leq \sum_{l=1}^{3N-q} E_{zpe,l}. \tag{28}$$

That is, whenever the sum of instantaneous mode energies is less than or equal to the sum of local vibrational mode energies, we re-scale the momenta. We do this in the following way. For those modes that dip below their zero-point energy, the normal mode momenta are re-defined to compel zero-point maintenance:

$$P_l' = \mathrm{sgn}(P_l)\sqrt{\Omega_l - \left(\frac{D_l}{\Omega_l}\right)^2}. \tag{29}$$

Total energy conservation is ensured by scaling the momenta of the other (non-violating) modes:

$$P_l' = \beta P_l, \tag{30}$$

where,

$$\beta = \sqrt{\frac{\sum_{l=1}^{3N-q} P_l^2 - \sum_{l=1}^{nvio} P_l'^2}{\sum_{l=nvio+1}^{3N-q} P_l^2}}, \tag{31}$$

Distribution A: Approved for public release; distribution unlimited.

and where *nvio* is the number of zero-point energy violating modes. We note that there must be enough momenta in the non-violating modes to achieve a rescaling (β must be real and greater than zero).

The last steps in the procedure involve transforming back from the projected space (*P'*) to the Cartesian space (*p'*). This is done using Eq. 29 of McCormack and Lim,[25]

$$\bar{p}'_\alpha = (\bar{\omega}_\alpha \times \bar{x}_\alpha) + \sum_{l=1}^{3N-q} P'_l \, \bar{\bar{L}}_l^{proj}(\alpha), \tag{32}$$

where $\bar{\omega}_\alpha$ is the angular velocity of atom α. Finally, we note that due to numerical round-off and putting a non-zero energy limit on the allowed vibrational modes, there will be some small energy error due to this final transformation. So we make a final scaling of the Cartesian momenta, defining the scaling factor, γ,

$$\gamma = \sqrt{\frac{KE}{KE'}}, \tag{33}$$

where *KE* is the total kinetic energy before and *KE'* is the total kinetic energy after enforcing zero-point maintenance. So that the final Cartesian momenta are:

$$\bar{p}''_\alpha = \gamma \, \bar{p}'_\alpha. \tag{34}$$

This final scaling is usually very small, perhaps one part in 10^5. However, with trajectories with tens of thousands of time steps, these small errors can mount up and become large. To further ensure that the zero-point algorithm does not perturb the system too much, we restrict the value of γ to be between 0.99 and 1.01 in a single time step.

4. Histogram and Gaussian binning

We follow the approach discussed in Czako and Bowman[32] and Bonnet and Rayez,[16] and extend it slightly to incorporate reactive collisions where several product channels are possible. The Gaussian binning approach starts with the expression for the vibrationally resolved cross section to state ν:

$$\sigma_\nu = \pi b_{max}^2 P_r P_\nu, \tag{35}$$

where b_{max} is the maximum impact parameter. In the above equation,

$$P_r = \frac{N_r}{N_{traj}}, \tag{36}$$

is the probability of particular reaction channel, where N_r is the number of trajectories which correspond to a particular reaction channel (such as collisional excitation) and N_{traj} is the total number of trajectories. For conventional 'histogram binning' (HB), P_ν is defined,

$$P_\nu^{HB} = \frac{N_\nu}{N_r}, \tag{37}$$

Distribution A: Approved for public release; distribution unlimited.

where N_ν is the number of trajectories whose product ends up in particular vibrational state ν. This gives the regular expression for the conventional histogram binning (HB) cross section:

$$\sigma_\nu^{HB} = \pi b_{max}^2 \frac{N_\nu}{N_{traj}}, \tag{38}$$

where the 'weight' of each trajectory is equal to 1.0. The Gaussian binning approach redefines the probability of a particular state in terms of Gaussian weights. So that

$$P_\nu^{GB} = \frac{\sum_{p=1}^{N_\nu} G_p(\nu)}{\sum_{s=1}^{N_s} \sum_{p=1}^{N_\nu} G_p(\nu)}, \tag{39}$$

where

$$G(\nu) = \frac{\beta}{\sqrt{\pi}} e^{-\beta^2 (\frac{(E(\nu')-E(\nu))}{2E(0)})^2}. \tag{40}$$

In the above equations, N_ν is the number of trajectories going to a vibrational product state ν, N_s is the number of product vibrational states, $E(\nu')$ corresponds to the energy of the vibrational state at the end of a trajectory and $E(\nu)$ corresponds to that energy where the quantum number is exactly an integer value. So the quantity $E(\nu')$-$E(\nu)$ corresponds to the 'distance' away from the true integer quantum state. The parameter β is the width of the Gaussian weight, and is set at a value of 16.651 so that the width of the weighting function is 0.1 out of 1.0 (FWHM).

5. Rotational quantum numbers and diatomic vibration

For the rotational quantum numbers of diatomic and polyatomic products, *J*, we use the convention:

$$J = |\bar{J}_r| - 1/2\,, \tag{41}$$

where $\bar{J}_r$, is the angular momentum vector. In principle, it may be possible to determine (*JKaKc*) resolved cross sections for H_2O products, as shown in the work of Ref. 13. In the present work, we do not follow the products long enough in time to make a meaningful estimate of the *Ka* and *Kc* quantum numbers. For determining OH diatomic vibrational quantum numbers we evaluate the integral for the semi-classical action, following standard procedures.[29]

C. Classical dynamics calculations

QCT calculations using a classical dynamics code written by the authors were performed using the BRSG surface and the three lowest triplet CBBB surfaces. In the calculations, the initial relative orientation of the O + H_2O complex was randomly chosen according to Ref. 33 with an initial separation between H_2O and O of 17.0 au. and a maximum impact parameter of 7.56 au. For these calculations, the

Distribution A: Approved for public release; distribution unlimited.

H_2O molecule is in the ground vibrational state with only the zero point normal mode vibrational energy and no rotational energy. The simulation time step was $1x10^{-16}$ s and a velocity-verlet integrator was used. Collision energies included 2, 4, 6, and 8 km s^{-1} for the BRSG surface and 2, 4, 6, 8, and 10 km s^{-1} for the CBBB surfaces. Products were declared when bond distances and angles matched equilibrium values within a specified criterion and were separated from each other by more than 17.0 au. Trajectories were then continued and product analysis occurred for $5.12x10^{-14}$ additional seconds. Using these procedures, products of all trajectories were successfully assigned for the CBBB surfaces at 8 km s^{-1}. For the BRSG surface at 8 km s^{-1}, about 0.1 % of the trajectories failed by either very poor energy conservation and/or dissociating to products other than O + H_2O, while at 2 km s^{-1} all trajectories on the BRSG surface were successful. It is known that the BRSG surface starts to fail at energies greater than 8 km s^{-1} which could likely be due to the surface deficiency shown in Figure 1c, and we may be accessing some of those geometries. Average energy conservation defined as the average of the energy change magnitude between the start and stop of a trajectory at 8 km s^{-1} was 0.19 kcal mol^{-1} for the BRSG surface and $6.8x10^{-5}$ kcal mol^{-1} for the lowest CBBB surface. For the CBBB surfaces, cross section results at a single velocity for each electronic state were summed and divided by three. Table I lists these and other simulation parameters. Table II lists vibrational frequencies and equilibrium geometries of reactants and products for each surface and literature values.

Simulations were run both with and without zero point maintenance, as described earlier. The zero-point maintenance simulations were run in two ways: with zero-point maintenance for the product analysis only (ZP1), and with zero-point maintenance enforced during the entire trajectory (ZP2). We defined an energy lower limit of 50 cm^{-1}; if a vibrational mode had less than this energy, it was not assigned as a vibration. For ZP2 simulations, it was necessary to define a force threshold. If the Hessian matrix elements between atoms exceeded this threshold, they were considered part of the same molecule when zero-point procedures were applied. Product analysis and zero-point maintenance required the calculation of a matrix of potential energy second derivatives (Hessian). Depending on the complexity of the potential, calculation of the Hessian could drive needed computer resources. At 8 km s^{-1}, it was found that without zero point maintenance, calculation of the Hessian for product analysis alone could take as long as the trajectory itself. Zero-point maintenance through the whole trajectory (ZP2) could increase the needed computer resources by two times or more compared to ZP1 calculations. It was found that enforcing zero-point maintenance for separated products only versus separated reactants and products did not change results, and saved considerable computer time.

Distribution A: Approved for public release; distribution unlimited.

III. QCT Results Using the BRSG Surface

In this section, results of QCT calculations using the BRSG surface are discussed, focusing on collisional excitation of H_2O fundamental vibrational modes (Eq. 4). Figure 2 shows the present calculated cross sections versus velocity along with previous calculations[7,9] using this surface and a measurement at 4.3 km s^{-1} for the bending and asymmetric stretch.[6] The present results, computed at 2, 4, 6, and 8 km s^{-1} collision velocity (4.1, 16.2, 36.5, and 64.8 kcal mol^{-1} collision energy), are shown as three lines with symbols within each panel. Each colored line uses a different method to find the vibrational quantum number: "QCT ACT" (black) uses the Fourier transform method of Schatz and co-workers to find the vibrational action,[15] "QCT HA" (red) uses the harmonic approximation of Rhee and Kim,[30] and "QCT EM" (blue) uses the elimination method of Rhee and Kim.[30] The top row of four panels is for exciting the fundamental bend. The middle row panels are for exciting the fundamental symmetric stretch. The bottom row panels are for exciting the fundamental asymmetric stretch. For a given row, each panel shows the present results for a different method of binning or zero-point maintenance: "ZP0" is the baseline QCT method and refers to conventional histogram binning and no zero-point maintenance algorithm employed, "ZP1" uses conventional histogram binning and enforces zero-point maintenance in the product analysis step, "ZP2" uses conventional histogram binning and enforces zero-point maintenance during the entire trajectory, and "GB" uses Gaussian binning and no zero-point maintenance. The statistical error for these calculations is less than 1% for cross section values above $5.x10^{-21}$ m^2 and about 10% for cross sections at $5.x10^{-23}$ m^2. However, by $5.x10^{-24}$ m^2 the statistical error is about 30 %. Results at or below this cross section value are therefore not meaningful. Furthermore, the Gaussian binned results suppress many trajectories, so the effective uncertainty is greater than described above. The two results labeled "QCT" (purple) are from Ref. 7, which use the same approximations as the baseline histogram binning and no zero-point algorithm case ("ZP0" "QCT ACT") and the same surface, but are run with 5,000 trajectories, an initial rotational energy of 0.08 eV = 1.8 kcal mol^{-1}, and a maximum impact parameter of 5.3 au. For the QCT results of Ref. 7, the purple line with symbols represents tabulated results, and the purple line with no symbols shows results obtained by fitting to a functional form as shown in Figures 1 and 2 of Ref. 7. The quoted statistical error is about 5-10 % for the fundamental bend mode and about 20-25 % for the fundamental stretch modes. The results labeled VCC-IOS (green line with symbols) are from approximate quantum scattering calculations of Johnson using the same BSRG surface.[9]

We first discuss the present QCT results for the bend excitation (top row of Figure 2) and evaluate the zero-point maintenance algorithms and binning methods. The chief result is that there is a dramatic lowering of the cross section especially at lower velocities, over two orders of magnitude at 4

Distribution A: Approved for public release; distribution unlimited.

km s^{-1}, in going from the ZP0 to the ZP1results and from the ZP0 to the GB results. The ZP1 and GB results generally match each other well. Examination of individual trajectories leading to bending excitation shows that the large bending ZP0 cross sections at low velocities mainly result from the borrowing of stretch mode vibrational energy which goes below zero-point values. Maintaining zero-point energy in the product region with ZP1 mostly corrects this problem. The GB results also suppress trajectories which borrow energy from stretching modes that go below zero-point. The ZP2 cross section matches the ZP1 and GB results fairly well at 6 km s^{-1} and 8 km s^{-1}, but remains un-physically large near threshold. (We note that at 2 km s^{-1}, there is not enough collision energy to allow excitation of the bending mode, without borrowing from zero-point stretches. Non-zero cross sections for bending excitation at these velocities are good indicators of a deficiency with the QCT method used.) For ZP2 trajectories leading to bending excitation at lower velocities, it was found that in the strong interaction region where the O and H_2O are near each other, very low frequency vibrations of the O + H_2O complex were highly excited. Before the products entered the O + H_2O product region, the low frequency modes would transfer energy to the bending vibration leading to bending excitation for a few trajectories, enough to boost the cross section at 2 km s^{-1} and 4 km s^{-1} to relatively large values. The interpretation of this was that internal rotation motion of the O + H_2O complex was being mistakenly changed into bending vibration of the H_2O through our particular implementation of the zero-point maintenance algorithm with ZP2 procedures. It may be possible to exclude these low frequency modes by setting a higher energy cutoff for counting vibrational modes. However, it was difficult in practice to implement a satisfactory cutoff for the entire trajectory which did not exclude what was obviously the H_2O bend vibration.

There are systematic differences between the QCT HA, QCT EM, and QCT ACT results. Although the QCT EM mode energies at any given time step are more accurate than the QCT HA mode energies, the QCT EM mode energies tend to undershoot the true mode energies for the fundamental modes. This behavior follows from the forms of the EM and HA potential energies. The errors for the QCT HA mode energy were generally unbiased, so the QCT HA averaged estimates are probably more accurate than the QCT EM results, at least for the fundamental modes. In general, the QCT HA and QCT ACT results agreed well for cross section values with a small statistical uncertainty. For these reasons we will therefore focus mainly on the QCT ACT results with ZP1 or GB, noting cases where they differ from each other.

In principle, the present QCT ACT results with ZP0 (conventional histogram binning) use the same methods as Redmon *et al.*[7] and the results should be directly comparable. The present results for ZP0 (conventional histogram binning) only match the results of Redmon *et al.*[7] at 8 km s^{-1}. The present ZP0 results are smaller than those of Redmon *et al.*[7] at lower velocities by up to a factor of 4 or 5 for the

Distribution A: Approved for public release; distribution unlimited.

bending mode, much larger than statistical uncertainty would allow. Indeed, for excitation of the stretching modes these differences are much larger. We attempted to exactly duplicate the Ref. 7 calculations by running 5,000 trajectories at 4 km s^{-1} with the same impact parameter and initial rotational energy following Ref. 7. The resulting fundamental bend cross section went from $4.1x10^{-21}$ m^2 using our original parameters in Table I to $2.4x10^{-21}$ m^2 with the parameters (maximum impact parameter and initial rotational energy) of Ref. 7. Although the new value agrees even less well with Ref. 7, this difference is on the order of the statistical uncertainty of the 5,000 trajectory run. It is possible that our reconstruction of the BSRG surface is in error. Other than this possibility, we are at a loss to explain the sometimes large differences between the present ZP0 ACT results and those of Ref. 7, especially for the stretching excitation cross sections.

On other hand, the QCT ACT ZP1 and QCT ACT GB cross sections agree well with the approximate quantum scattering cross sections of Ref. 9 using the same BSRG surface. This level of agreement between QCT GB and quantum scattering cross sections has been seen in other systems.[34] For O + H_2O bending excitation, the GB and ZP1 approaches properly correct for an extremely large deficiency in conventional QCT methods. We have attempted to optimize the value of the weighting width parameter, β, used in the GB calculations to better agree with the quantum scattering results of Ref. 9. Better agreement can be achieved at velocities of 4 km s^{-1} and higher. However, this improvement comes at the expense of increased cross sections at 2 km s^{-1}, which are not strictly allowed. Finally, we note that the results of Dunn et al.[6] are more than 10 times greater than the quantum scattering results of Ref. 9 and the present QCT results GB and ZP1 results.

Figure 2 also shows cross sections for exciting the fundamental symmetric stretch and asymmetric stretch modes. The present QCT stretching cross sections at all levels of theory are much smaller than the present bend cross sections. For the stretches, the difference between conventional QCT ZP0 and QCT ZP1/GB results are much smaller than for exciting the bend. For the asymmetric stretch, the QCT EM result lies about an order of magnitude below the QCT HA and QCT GB results, and we believe this is due to the systematic underestimate of the QCT EM mode energy, mentioned earlier. The present QCT ACT and QCT HA results with ZP1 and GB0 are within a factor of two or three of the approximate quantum scattering results using the same surface of Ref. 9 near 8 km s^{-1}. At 6 km s^{-1} the present results are zero within the statistical error, and clearly more trajectories are needed to make a meaningful comparison at this velocity. The difference between the QCT results of Ref. 7 using the same surface and the present results is large, amounting to more than an order of magnitude at 8 km s^{-1}, and by inference several orders of magnitude at lower velocities. However, at 4.3 km s^{-1}, the results of Dunn *et al.*[6] for the asymmetric stretch have fair agreement with the QCT results of Ref. 7. Taken together, our

Distribution A: Approved for public release; distribution unlimited.

impression is that the consistently good agreement between the present QCT ZP1/GB results and the approximate quantum scattering results for all fundamental modes indicates that our implementation of the BSRG surface is likely correct, and that either a QCT ZP1 or GB approach can correct for deficits in conventional QCT methods.

To help understand the present QCT approaches at a deeper level, Figure 3 shows contours of the probability for exciting bend and stretch modes as a function of the classical vibrational action for the ZP0, ZP1, and ZP2 approaches at 2, 4, and 8 km s^{-1} collision velocities. The log10 of the probability contour values, normalized so that each sub-panel sums to 1.0, are shown over a very large dynamic range to highlight low value cross sections. The symmetric and asymmetric stretching actions have been averaged to a single effective stretch mode action for ease of viewing. The ZP0 panel results show that the probability of exciting the bending mode (actions > 0.5) derives mainly from trajectories which have borrowed energy from the stretch modes, which dip below actions equal 0.0. From these plots, it is clear how the ZP1 algorithm reduces the amount of bending excitation. Gaussian binning, which effectively multiplies these probabilities by peaked functions at integer values of the actions, achieves a similar effect. It is also clear that at 4 km s^{-1} and to some extent at 2 km s^{-1}, the ZP2 results start to allow the borrowing of stretch mode zero-point to excite the bend, which had been suppressed in the ZP1 results.

Figure 4 gives a different view of the vibrational cross sections. Figure 4a gives vibrational energy distributions binned at 2 kcal mol^{-1} for the 4 collision velocities studied for ZP1. These distributions are peaked near the zero-point energy of H_2O at 13.6 kcal mol^{-1} (for the BRSG potential) and fall off rapidly with energy. Even with zero-point maintenance (and Gaussian binning), there are many trajectories which fall below the H_2O zero point energy, giving rise to non-zero cross sections below the peak at 13.6 kcal mol^{-1}. As the collision velocity increases, the width of the distribution around the zero point increases, especially at 8 km s^{-1} where there is a high energy tail extending up to 30 kcal mol^{-1}. The increasing width of the distributions indicates increasing vibrational excitation with velocity, but gives little quantitative information. Figure 4b shows vibrationally state-resolved cross sections at 6 and 8 km s^{-1} versus vibrational energy. At 8 km s^{-1}, there appears to be an exponential fall-off of the cross section with vibrational energy, which is consistent with an energy gap law. Figure 4c shows the angular distribution cross sections for the ground state and fundamental vibrationally excited modes. For vibrational excitation, the H_2O is clearly back-scattered, which is consistent with a picture of a hard collision.

Figure 5 gives an overview of the calculated rotational distributions for O + H_2O collisions. Figure 5a gives the cross section of low-lying H_2O J levels summed over all vibrational levels over a wide energy

Distribution A: Approved for public release; distribution unlimited.

range. As indicated, below ~4 kcal mol^{-1} results from Schwenke[28] are shown for comparison. Schwenke used a slightly modified BSRG potential and did not include H_2O vibration. There are three results shown for the Schwenke study: standard classical dynamics (symbols without lines), full quantum scattering (symbols with solid lines), and approximate quantum scattering (symbols with dotted lines). The three Schwenke approaches are very close and cannot be easily distinguished on the scale of the figure, except for the J=1 level, where the standard classical results overestimate the quantum cross sections by a little over a factor of two. Although they do not overlap in energy, the present results are consistent with the corresponding QCT calculations of Schwenke. Figure 5b shows calculated J-resolved cross sections for QCT ACT and Gaussian binning at the 4 collision velocities studied, summed over all vibrational levels. At the highest collision energy, J-levels of 30 and above are populated. Figure 5c shows ro-vibrationally resolved cross sections for the ground and fundamental vibrational levels at 8 km s^{-1}. The (000) J-resolved cross section falls off fairly rapidly with energy; the (010) cross section is much flatter versus J-level, with a maximum near J=5 and gentle fall-off until there is a cutoff around J=30. The statistics for the stretching resolved J-cross sections are poor, but give some indication that they are relatively flat with J-level. The vibrationally resolved rotational energy distributions at 8 km s^{-1} are shown in Figure 5d. For any single rotational energy bin, there are several J levels which contribute. This creates a rolling average of the J-resolved cross sections seen in Figure 5c. For the (000) and (010) levels, except for the lowest energy bin, the distributions fall off with an energy gap type of behavior. For the stretching modes, again the statistics are poor, but the rotational energy distribution is flat.

IV. QCT Results Using the CBBB surfaces

A. Ro-vibrational excitation of H_2O

In Figure 6, cross sections for excitation of the H_2O fundamental vibrational modes are shown using the CBBB surfaces. Several results are shown including those shown previously using the BRSG surface and Gaussian binned. For the CBBB results, the statistical error in the cross sections (1 σ) is approximately 13% at $1.x10^{-22}$ m^2 and 41% at $1.x10^{-23}$ m^2. The experimental results of Dunn *et al.*[6] are shown as well as the QCT results of Redmon and Schatz[7] and the approximate quantum scattering calculations of Johnson,[9] both of which utilize the BRSG surface.

Examining the bending excitation cross sections, the present QCT ZP0 results are un-physically large and remain at a near-constant value over the entire velocity range. As with the BRSG ZP0 result, these large cross sections are due to borrowing zero-point energy from the stretching modes. Maintaining zero-point energy (ZP1 and ZP2 curves which we have suppressed for clarity) considerably lowers the cross section. Likewise, the GB approach corrects for this zero-point energy borrowing deficiency. At 6

Distribution A: Approved for public release; distribution unlimited.

and 8 km s^{-1}, the CBBB GB and BRSG GB bending excitation cross sections agree well. Closer to threshold, the BRSG GB cross section is a factor of 3-5 larger than the CBBB GB cross section, but the statistics here are relatively poor. Both the CBBB GB and BRSG GB cross sections agree fairly well with the approximate quantum scattering results of Johnson,[9] except at 2 km s^{-1}, where the classical results over-estimate the cross section. The present GB results with both surfaces and the approximate quantum scattering results are all about 10 times smaller than the measurement of Dunn *et al.*[6]

Figure 6 also shows results for the stretching vibrations. Here the picture is more complex. The correction in going from the ZP0 to GB result for the symmetric stretch cross section is large, and for the asymmetric stretch it is very small. We found that the large ZP0 symmetric stretch cross section is due to a just a few trajectories on the S3 (highest energy) CBBB surface. The S3 surface is the only one that does not contain an H + OOH channel, and symmetric stretching may be sensitive to this difference. Gaussian binning completely suppresses these trajectories. However, the statistical uncertainties for the symmetric stretch CBBB result are large. For the CBBB GB result, the asymmetric stretch cross section is much larger than the symmetric stretch. For the BRSG surface the symmetric and asymmetric stretch cross sections are comparable. For both the stretches, the difference between the CBBB and BRSG surface cross sections are about a factor of 4 or 5. The stretch excitations are more sensitive than bending to differences in the non-reactive versus reactive potential, as these modes sample the breaking and formation of bonds during reaction. The measurement of Dunn *et al.*[6] for the (001) cross section at 4.3 km s^{-1} is at least several orders of magnitude above the present results.

Figure 7a shows H_2O vibrational distributions. The peak of the distributions occurs at the H_2O zero point energy. Vibrational energy in excess of 30 kcal mol^{-1} is observed at high collision velocity (8 and 10 km s^{-1}). Figure 7b shows the state-resolved vibrational cross sections as a function of the vibrational energy. At the highest collision velocities an exponential fall-off of the cross section with vibrational energy is observed. Figure 7c shows the differential angular cross sections for the ground and fundamental vibrational modes at 8 km s^{-1} using the GB method. For the ground state, the H_2O is strongly forward scattered and is mostly backscattered for the fundamental vibrations. The results for the (100) mode are not statistically significant and so we do not show them here.

In Figure 8a, the rotational cross sections for H_2O are shown as a function of the H_2O rotational angular momentum, J, using the CBBB potential. These have been summed over all vibrational states. QCT ACT GB results are shown. Similar to the results of the BRSG potential, as the collision velocity increases, the higher rotational states are populated, with significant rotational cross sections above J=20 at 6, 8 and 10 km s^{-1}. At collision velocities of 2 and 4 km s^{-1}, the distribution of the J states differs

Distribution A: Approved for public release; distribution unlimited.

slightly from the BRSG calculated distributions. With the CBBB surfaces, there are more states populated between J=5 and J=10. Slight differences in the potential surfaces could be the source of such differences, especially for these low energy excitations where the rotational energies for J<10 are less than 5 kcal mol^{-1}. In Figure 8b, the ro-vibrationally resolved cross sections are given for the ground and (010) and (001) vibrations at 8 km s^{-1} using the QCT ACT GB method. The (000) cross section decreases monotonically with J, but the (010) cross section peaks near J=10, while the (001) cross sections are relatively flat with J. Figure 8c shows the rotational energy distributions for the ground and the (010) and (001) modes. Except for the lowest energy bin, these show an exponential fall-off with energy consistent with an energy gap law.

B. Reactive cross sections

In Figure 9a, the reactive cross sections are shown for processes in Eqs. 1-3: OH formation, H elimination, and O atom exchange. We have discussed these cross sections in detail in [3,5]. Briefly, the OH + OH reaction dominates the reactive cross section at low collision velocities. When the collision energy increases above the activation barrier for H elimination at 8 km s^{-1}, the cross section for the H + OOH reaction becomes significant and competitive with the hydrogen abstraction reaction at 10 km s^{-1}. The O-atom exchange process has a relatively low barrier (33 kcal mol^{-1}) and turns on at 6 km s^{-1}. The opacity function is given for each of the reactions at a collision velocity of 10 km s^{-1} in Figure 9b. The opacity function, *P(b)*, has the following relation to the cross section, σ, : $\sigma = \int_0^{b_{max}} P(b) b db$, where *b* is the impact parameter and b_{max} is the maximum impact parameter. Low impact parameters correspond to O-atom interaction in close proximity to the H_2O center of mass. With sufficient energy at 8 km s^{-1}, these low impact parameter interactions tend to lead to the H + OOH product channel. As the impact parameter decreases, the probability of the H + OOH channel increases indicating a 'direct' interaction is necessary. The hydrogen abstraction reaction, however, occurs at larger impact parameters; the formation of OH + OH dominates the cross section at impact parameters greater than ~1 au. The opacity function for the O-atom exchange reaction is similar to that of the H + OOH reaction albeit two orders of magnitude lower. This indicates that exchange reaction requires a low impact parameter between the O and H_2O and in addition is limited to particular geometries.[5] For these total reaction cross sections, differences between ZP0, ZP1, and ZP2, and GB results were very small.

We now examine the ro-vibrationally resolved cross sections and product energy distributions of the OH formation and H elimination reactive channels. Statistics for the ro-vibrationally resolved O-atom exchange channel were too poor to present results for this channel. Results for QCT ACT with Gaussian binning (GB) will be shown. Very near threshold the ZP0 results produced small cross section products

Distribution A: Approved for public release; distribution unlimited.

that were only energetically allowed by borrowing zero-point energy. Besides this, differences between ZP0, ZP1, ZP2, and GB results were generally small.

1. OH+OH reaction

The vibrational energy distributions for the OH + OH products are shown in Figure 10a. The contributions for each OH product has been summed and divided by two, so the integrated distribution at a given collision velocity equals the reactive cross section. The distributions peak near the zero point of OH near ~5 kcal mol^{-1}. At the highest collision velocities examined, cross sections are observed at vibrational energies in excess of 20 kcal mol^{-1}. Beyond the zero-point peak, this energy distribution falls off approximately exponentially. This is more clearly seen in Figure 10b, which shows the vibrationally resolved cross section versus vibrational energy, where again the two product OH cross sections are summed and divided by two. In a previous study,[35] we have shown that two distinct types of OH products are formed. A spectator OH, corresponding to the OH H_2O bond that is not broken, occurs with lower vibrational and rotational energy, and an active OH, corresponding to the OH bond that is newly created, is formed with higher vibrational and rotational energy. This bi-modal behavior can be seen in the Figure 10b, where after the OH(v=0) peak, there is an exponential fall-off of the vibrational energy. However, the OH(v=0) level rises above this exponential line for a given collision velocity. This is due to the contribution of the OH spectator which is formed mostly in the v=0 state, while the active OH is formed with a wide distribution of vibrational levels.

The rotationally resolved cross sections for OH are shown in Figure 11 where contributions from both OH products have been summed and divided by 2. In Figure 11a we show the J-resolved distributions summed over vibrational levels. At the higher collision velocities, these distributions are actually sums of a spectator OH distribution peaked at low J (between J=5 and 10) and an active OH distribution which is broad with a higher J tail.[35] This can be seen in a different way in Figure 11b, which shows the J resolved cross sections at 8 km s^{-1} for the OH(v=0) and OH(v=1) levels. For OH(v=0), the peak near J=8 is due to the spectator OH and the higher energy J tail is due to the active OH. For OH(v=1), the J-resolved cross section has poor statistics. But the very broad distribution versus J is evident and is due mostly to active OH formed in the v=1 level. Figure 11c shows the rotational energy distributions at 8 km s^{-1}, for OH(v=0,1,2,3). At the highest collision velocity, these distributions extend beyond 20 kcal mol^{-1}. Above 5 kcal mol^{-1} they can be approximately described by an exponential fall off with energy. This view of the cross section in Figure 11c is basically a remapping for Figure 11b, where the low J values have been compressed to the lower energy bin and the higher J values are spread across widely to higher energy bins.

Distribution A: Approved for public release; distribution unlimited.

2. OOH + H reaction

Figure 12 shows the vibrationally resolved cross sections for the OOH product. To our knowledge this is the first time vibrationally resolved cross sections have been reported for this channel. Figure 12 shows the vibrational energy distributions for OOH at a collision velocity of 10 km s^{-1}, where we show the separate contributions from the X state of OOH (energy threshold of ~ 60 kcal mol^{-1})[3] and the A state of OOH (energy threshold of ~84 kcal mol^{-1}).[3] The zero-point energy of these states is about ~10 kcal mol^{-1}. In contrast to the vibrational distributions of H_2O and OH which are strongly peaked near their zero-point, the vibrational energy distribution for OOH is extremely broad. The X state, having a lower energy threshold, dominates the distribution and extends up to 40 kcal mol^{-1}. We have noted previously that the H elimination channel is unusual in that ~40% of available collision energy ends up in the internal energy of the OOH product.[5] The vibrationally resolved cross section is shown in Figure 12b, where the X state (which dominates) and A state contributions have been summed. The harmonic normal modes for the X state of OOH have energies of 3863.7(H-stretch), 1666.7(bend), and 1041.8 (O-O stretch) cm^{-1} [3], and we use the notation from high to low energy (H-stretch, bend, O-O stretch). The cross sections for the ground (000) and first excited bend (010) (which is not the lowest energy mode) modes are nearly equal, which is consistent with the broad vibrational energy distribution. Below values of $1x10^{-22}$ m^2 (which are not shown), there is excitation of a large number of states at higher vibrational energies, which make up the high energy tail of the X state vibrational energy distributions. These states have large statistical uncertainties and require many more trajectories to give a quantitative estimate of their cross sections. The angular distribution cross sections for the ground (000) and (001) and (010) states at 10 km s^{-1} are shown in Figure 12c. The angle is the center of mass scattering angle. High scattering angles correspond to scattering of the OOH product in the same direction as the reactant H_2O molecule. The dominant backscattering component for this channel has been seen previously.[1,3] Reaction takes place at small impact parameters (hard collisions).

In Figure 13a, we show the J-resolved cross section for the OOH product at 10 km s^{-1}. The cross section is summed over X and A states and all vibrational states. The J-resolved cross section has a broad distribution with significant populations from J=20 to J=70 and extends past J=100. The broad distribution extending to high J is due to two factors, the relatively large amount of energy deposited in internal motion and the rotational constants of OOH. The experimentally determined rotational constants for OOH (X state) are A=20.35, B=1.12, and C=1.06 cm^{-1}.[36] This corresponds to a near prolate symmetric top, with A > B ≈ C and energy levels $E_{rot,J} = BJ(J+1) + (A-B)K^2$, *K=J,J-1,…, -J*. Because of the relatively small value of the smallest rotational constants, for K=0 very large J values can be populated. Also, because of the large difference between the largest and smallest rotational constants, a

Distribution A: Approved for public release; distribution unlimited.

given J level can give rise to a large number of K states which span a large energy range. This is shown in Figure 13c, where rotational energy is plotted as a function of J. For rotational energies of 30 kcal mol^{-1} and lower, possible angular momentum states are possible up to J=100 for small K values. Figure 13b shows the rotational energy distribution summed over the X and A states and all vibrational states, which is nearly flat with rotational energy. This distribution is fundamentally different than the corresponding H_2O or OH distributions where the low energy population (< 10 kcal mol^{-1}) is at least an order of magnitude greater than the high energy population (> 10 kcal mol^{-1}).

3. Rate constant calculations

As a test on the CBBB potential, Figure 14 shows the computed rate constants versus temperature using the CBBB surfaces for the reactions of (a) $O + H_2O \rightarrow OH + OH$ and (b) $OH + OH \rightarrow H_2O + O$ along with measured data [20-23]. For the $O + H_2O$ rate constant, results using an older set of potential surfaces[35] using QCT are also shown. For the present CBBB results for the $O + H_2O$ rate constant, contributions from each of the three electronic states are summed and divided by 3. The CBBB result agrees well with the highest valued experimental measurement. For the OH + OH rate constant, contributions from each electronic state are multiplied by 1/4 to reflect the fact the OH + OH reactants are 4x degenerate. Our calculations neglect contributions from the fourth electronic state, but we have seen that the contribution from the 3rd highest state is negligible, so we expect that the fourth state we are leaving out does not contribute significantly. The present results agree fairly well with the highest valued measurements.

V. CONCLUSIONS

Classical dynamics calculations for $O(^3P) + H_2O(^1A_1)$ hyperthermal collisions were performed. Several methods were used to produce ro-vibrationally state-resolved product cross sections and to enforce zero-point maintenance from analysis of the classical trajectories. In one series of calculations, a non-reactive surface (BRSG)[7,8,18] used in past classical[7] and quantum collision studies[9] was used. Results with this surface for collisional excitation suggest that classical dynamics calculations which include Gaussian binning procedures and/or selected zero-point maintenance algorithms can produce results which approximate quantum scattering cross sections. Without these procedures, the classical cross sections can be many orders of magnitude greater than the quantum cross sections for exciting the bending vibration of H_2O, especially near threshold. This is due to energy borrowing from stretching modes which dip below zero-point values. In a second series of calculations, recently developed reactive $O(^3P) + H_2O(^1A_1)$ surfaces were used (CBBB).[3] For these surfaces the three lowest triplet states of the $O + H_2O$ system included reaction to form OH + OH, H + OOH, and O-atom exchange. For bending

Distribution A: Approved for public release; distribution unlimited.

vibrational excitation, results for the BRSG and CBBB surfaces agreed fairly well. For the stretches the cross sections showed differences of factors of 4 or 5, although the statistical uncertainties were large. The stretch excitations are more sensitive than bending to differences in the non-reactive versus reactive surfaces, as these modes sample the breaking and formation of bonds during reaction. The measurements of Dunn *et al.*[6] for the (010) and (001) cross sections at 4.3 km s^{-1} were at least an order of magnitude above the present results. For the reactive channels, the present calculations using the CBBB surfaces show that at higher velocities there is an unusually large amount of product internal excitation. For OOH, where 40% of available collision energy goes into internal motion, the excited product vibrational and rotational energy distributions are relatively flat. Other product channel distributions show an exponential fall-off with energy consistent with an energy gap law. The present detailed distributions and cross sections can serve as a guide for future hyperthermal measurements of this system.

ACKNOWLEDGEMENTS

The authors acknowledge support under contract number W9113M-10-C-0082. We also acknowledge George Schatz, Northwestern University, for technical help with the BRSG surface. Finally, we acknowledge Tom Smith of AFRL for technical guidance.

REFERENCES

1 A. L. Brunsvold, J. M. Zhang, H. P. Upadhyaya, T. K. Minton, J. P. Camden, J. T. Paci, and G. C. Schatz, J. Phys. Chem. A **111** (43), 10907 (2007).

2 B. Ruscic, A. F. Wagner, L. B. Harding, R. L. Asher, D. Feller, D. A. Dixon, K. A. Peterson, Y. Song, X. Qian, C.-Y. Ng, J. Liu, W. Chen, and D. W. Schwenke, J. Phys. Chem. A **106** (11), 2727 (2002).

3 P. F. Conforti, M. Braunstein, B. J. Braams, and J. M. Bowman, J. Chem. Phys. **133** (16), 164312 (2010).

4 B. Ruscic, R. E. Pinzon, M. L. Morton, N. K. Srinivasan, M.-C. Su, J. W. Sutherland, and J. V. Michael, J. Phys. Chem. A **110** (21), 6592 (2006).

5 M. Braunstein and P. F. Conforti, Chem. Phys. Lett. **523**, 34 (2012).

6 M. G. Dunn, G. T. Skinner, and C. E. Treanor, AIAA Journal **13** (6), 803 (1975).

7 M. J. Redmon, G. C. Schatz, and B. C. Garrett, J. Chem. Phys. **84** (2), 764 (1986).

8 R. J. Bartlett and M. J. Redmon, Report No. AFRPL-TR-81-27, 1981.

9 B. R. Johnson, J. Chem. Phys. **84** (1), 176 (1986).

10 G. Czako and J. M. Bowman, Science **334** (6054), 343 (2011).

11 J. D. Sierra, L. Bonnet, and M. Gonzales, J. Phys. Chem. A **115** (26), 7413 (2011).

Distribution A: Approved for public release; distribution unlimited.

[12] G. Czako, Y. Wang, and J. M. Bowman, J. Chem. Phys. **135** (15), 151102 (2011).

[13] A. Faure, L. Wiesenfeld, M. Wernli, and P. Valiron, J. Chem. Phys. **124** (21), 214310 (2006).

[14] J. M. Bowman, B. Gazdy, and Q. Sun, J. Chem. Phys. **91** (5), 2859 (1989); W. H. Miller, W. L. Hase, and C. L. Darling, J. Chem. Phys. **91** (5), 2863 (1989).

[15] G. C. Schatz, Comput. Phys. Commun. **51** (1-2), 135 (1988).

[16] L. Bonnet and J. C. Rayez, Chem. Phys. Lett. **277** (1-3), 183 (1997).

[17] L. Bonnet and J. C. Rayez, Chem. Phys. Lett. **397** (1-3), 106 (2004).

[18] M. J. Redmon and G. C. Schatz, Chem. Phys. **54** (3), 365 (1981).

[19] B. J. Braams and J. M. Bowman, Int. Rev. Phys. Chem. **28** (4), 577 (2009).

[20] D. L. Baulich, C. J. Cobos, R. A. Cox, C. Esser, P. Frank, T. Just, J. A. Kerr, M. J. Pilling, J. Troe, R. W. Walker, and J. Warnatz, J. Phys. Chem. Ref. Data **21** (3), 411 (1992).

[21] A. M. Lifschitz, J. V., Symp. Int. Combust. Proc. **23**, 56 (1991).

[22] W. Tsang and R. F. Hampson, J. Phys. Chem. Ref. Data **15** (3), 1087 (1986).

[23] M. S. Wooldridge, R. K. Hanson, and C. T. Bowman, Int. J. Chem. Kinet. **26** (4), 389 (1994).

[24] T. Shimanouchi, Report No. NSRDS NBS-39, 1972.

[25] K. F. Lim and D. A. McCormack, J. Chem. Phys. **102** (4), 1705 (1995).

[26] D. Bonhommeau and D. G. Thrular, J. Chem. Phys. **129**, 014302 (2008).

[27] K. S. Sorbie and J. N. Murrell, Mol. Phys. **29** (5), 1387 (1975).

[28] D. W. Schwenke, J. Phys. Chem. **97** (29), 7627 (1993).

[29] D. G. Truhlar and J. T. Muckerman, in *Atom-Molecule Collision Theory: A Guide for the Experimentalist*, edited by R. B. Bernstein (Plenum Press, New York, 1979), pp. 505.

[30] Y. M. Rhee and M. S. Kim, J. Chem. Phys. **107** (5), 1394 (1997).

[31] J. D. Louck and H. W. Galbraith, Rev. Mod. Phys. **48** (1), 69 (1976).

[32] G. Czako and J. M. Bowman, J. Chem. Phys. **131** (24), 244302 (2009).

[33] W. L. Hase, D. M. Ludlow, R. J. Wolf, and T. Schlick, J. Phys. Chem. **85** (8), 958 (1981).

[34] T. Xie, J. M. Bowman, J. W. Duff, M. Braunstein, and B. Ramachandran, J. Chem. Phys. **122** (1), 014301 (2005).

[35] M. Braunstein, R. Panfili, R. Shroll, and L. Bernstein, J. Chem. Phys. **122** (18) (2005).

[36] A. Charo and F. De Lucia, J. Mol. Spectrosc. **94** (2), 426 (1982).

[37] A. R. Hoy and P. R. Bunker, J. Mol. Spectrosc. **74** (1), 1 (1979).

[38] M. E. Jacox, in *NIST Chemistry WebBook, NIST Standard Reference Database Number 69*, *http://webbook.nist.gov*, edited by P. J. Linstrom and W. G. Mallard (National Institute of Standards and Technology, Gaithersburg, MD 20899, 2012).

Distribution A: Approved for public release; distribution unlimited.

[39] K. G. Lubic, T. Amano, H. Uehara, K. Kawaguchi, and E. Hirota, J. Chem. Phys. **81** (11), 4826 (1984).

[40] K. P. Huber and G. Herzberg, *Constants of Diatomic Molecules*. (Can Nostrand, Princeton, 1979).

Distribution A: Approved for public release; distribution unlimited.

TABLES

Table I. Parameters used in QCT calculations.

Parameter	Value
Collision velocities	2, 4, 6, 8 (BRSG) 2, 4, 6,8, 10 (CBBB) km s^{-1}
Maximum impact parameter	7.54 au, σ_{tot} = 1.78.60 au = 5.03x10^{-19} m^2
Initial separation	17.0 au
Number of trajectories per velocity	1.x10^6(BRSG), 1.x10^5 (CBBB per surface)
Statistical Uncertainty (1σ)	10% at 5.x10^{-23} m^2; 32% at 5.x10^{-24} m^2 (BRSG) 13% at 1.x10^{-22} m^2; 41% at 1.x10^{-23} m^2 (CBBB)
Time-step	1x10^{-16} s
Product analysis time	5.12x10^{-14} s
Maximum trajectory time	1.x10^{-11} s
Rotational energy bin width	2 kcal mol^{-1}
Translational energy bin width	2 kcal mol^{-1}
Vibrational energy bin width	2 kcal mol^{-1}
Angular bin width	10 degrees
z.p. lower limit	50 cm^{-1}
z.p. dV/dx^2 (energy/length^2) threshold	3.16x10^{-7} au (BRSG), 3.16x10^{-6} au (CBBB)
Average energy conservation (8 km s^{-1})	0.19 kcal mol^{-1} (BRSG) 6.8x10^{-5} kcal mol^{-1}(CBBB)

Distribution A: Approved for public release; distribution unlimited.

Table II. Frequencies (cm^{-1}) and equilibrium geometries (au, radians) of reactants and products. The BRSG and CBBB frequencies are harmonic frequencies determined from these surfaces. The literature value frequencies are derived from measurements for excitation of fundamental modes and therefore include anharmonic and higher order contributions.

Molecule	BRSG and CBBB Surfaces	Literature
H_2O	Freq.=3863.7, 1688.1, 3973.2 (BRSG) R_{OH}= 1.81, θ_{HOH} =1.83 (BRSG) Freq.= 3753.5 ,1781.4,3760.5 (CBBB) S1 R_{OH}=1.83, θ_{HOH} =1.81 (CBBB) S1	Freq.=3657, 1595, 3756 [24] R_{OH} =1.81 , θ_{HOH} =1.82 [37]
OOH	Freq.= 3863.7, 1666.7, 1041.8 (CBBB) S1 (X) R_{OO}=2.56, R_{OH}=1.83, θ_{OOH} =1.77	Freq.=3436, 1392, 1098 [38] R_{OO} =2.51, R_{OH} =1.8, θ_{OOH} =1.82[39]
OH	Freq. = 3859.9 (CBBB) S1 R_{OH}= 1.85	Freq.=3738 [40] R_{OH} =1.83 [40]

Distribution A: Approved for public release; distribution unlimited.

FIGURE CAPTIONS

Figure 1. Potential energies for $O(^3P) + H_2O(^1A_1)$ using the BSRG surface of Refs. 7, 8, and 18 and the CBBB S1 surface of Ref. 9. In (a) and (b) H_2O is held near its equilibrium geometry R_{OH}=1.83 au, θ_{HOH} =1.82 rad and the O-atom is moved in the H_2O plane. In (c) and (d) the H_2O geometry corresponds to bond lengths of R_{OH1}=1.83au and R_{OH2}=2.40 au, and an angle θ_{HOH} =1.82 rad. The O-atom is moved in the H_2O plane.

Figure 2. Fundamental vibrational excitation cross sections for O + H_2O collisions using the BRSG surface. Please see text for description of data.

Figure: 3 Contour plots of the log10 of the vibrational excitation probabilities normalized to 1.0 for each sub-panel versus the bending and averaged stretching vibrational actions using the BSRG surface.

Figure 4: Vibrational cross sections for O + H_2O collisions with the BSRG surface: (a) Vibrational energy distribution cross sections (m^2/kcal mol^{-1}) at 2, 4, 6, and 8 km s^{-1} for QCT ZP1. (b) Vibrational excitation cross sections at 8 km s^{-1} and 6 km s^{-1} for QCT GB. (c) Angular distribution cross sections for the ground and fundamental H_2O modes at 8 km s^{-1} for QCT GB.

Figure 5: Rotational cross sections for O + H_2O collisions with the BSRG surface. (a) J-resolved cross sections versus collision energy; below 4 kcal mol-1, results are shown from Ref. 28, (b) J-resolved cross sections at a number of collision velocities, (c) J-resolved cross sections for the ground and vibrational fundamental modes at 8 km s^{-1}, (d) Rotational energy distributions for the ground and vibrational fundamental modes at 8 km s^{-1}.

Figure 6: Vibrational excitation cross sections for O + H_2O collisions. (a) excitation to the (010) state (b) excitation to the (100) state, (c) excitation to the (001) state. Black line with circles (CBBB GB) denotes Gaussian binned results using the CBBB surfaces; Red line with squares (CBBB ZP0) denotes conventional histogram and no zero-point algorithm using the CBBB surfaces; Blue line with triangles (BRSG GB) denote present QCT Gaussian binned results using the BRSG surface; Purple lines denote results from Ref. 7; Purple lines with symbols are tabulated; Purple lines without symbols are a function fit; Green lines with diamonds (VCC-IOS) are the approximate scattering results Johnson[9]; Cyan blue symbols (Dunn *et al.*) are shock tube measurements from Dunn *et al.*[6]

Figure 7: Fundamental vibrational cross sections for O + H_2O collisions with the CBBB surfaces: (a) Vibrational energy distribution cross sections (m^2/kcal mol^{-1}) at 2, 4, 6, 8, and 10 km s^{-1} for QCT ZP1. (b)

Distribution A: Approved for public release; distribution unlimited.

Vibrational excitation cross sections at 6, 8, and 10 km s^{-1} for QCT ACT GB. (c) Angular distribution cross sections for the (000), (010), and (001) H_2O modes at 8 km s^{-1} for QCT ACT GB.

Figure 8: Rotational cross sections for O + H_2O collisions with the CBBB surfaces leading to excited H_2O. (1) J-resolved cross sections at a number of collision velocities, (b) J-resolved cross sections for the (000), (010), and (001) modes at 8 km s^{-1}, (c) Rotational energy distributions for the (000), (010), and (001) modes at 8 km s^{-1}.

Figure 9: (a) The total reactive cross sections versus collision velocity (b) The opacity function versus impact parameter at 10 km s^{-1} for each reactive channel.

Figure 10: Vibrational cross sections for formation of OH + OH using the CBBB surfaces. (a) Vibrational energy distributions. (b) Vibrationally resolved cross sections.

Figure 11: Rotational cross sections for O + H_2O collisions with the CBBB surfaces leading to OH + OH. (a) J resolved cross sections summed over vibrational states. (b) The ro-vibrationally resolved cross section ground and first excited states at 8 km s^{-1}. (c) Rotational energy distributions for OH(v=0,1,2,3,4) at 8 km s^{-1}.

Figure 12: Vibrational cross sections for O + H_2O collisions with the CBBB surfaces leading to H + OOH. (a) Vibrational energy distributions for the X and A states of OOH at 10 km s^{-1}. (b) Vibrationally resolved cross sections 10 km s^{-1}. (c) The differential angular cross section for the (000), (001), and (010) states at 10 km s^{-1}.

Figure 13: Rotational cross sections for O + H_2O collisions with the CBBB surfaces leading to H + OOH. (a) J-resolved cross section for OOH at 10 km s^{-1} (b) Rotational energy distributions of OOH at 10 km s^{-1}. (c) Rotational energy of OOH as a prolate symmetric top versus J.

Figure 14: (a) Rate constants for the reaction of O + $H_2O \rightarrow$ OH + OH in m^3 $molecule^{-1}$ s^{-1} as a function of temperature in Kelvin. The legend notation is as follow: JCP2010 are the present CBBB results. JCP2005 are the results of Ref. 35. LIF 1991 is from Ref. 21. TSA 1986 is from Ref. 22. (b) Rate constants for the reaction of OH + OH $\rightarrow$ O + H_2O in m^3 $molecule^{-1}$ s^{-1} as a function of temperature in Kelvin. JCP 2010 are the present CBBB results. WOO 1995 is from Ref. 23. BAU 1992 is from Ref. 20. TSA 1986 is from Ref. 22.

Distribution A: Approved for public release; distribution unlimited.

FIGURES

Figure 1

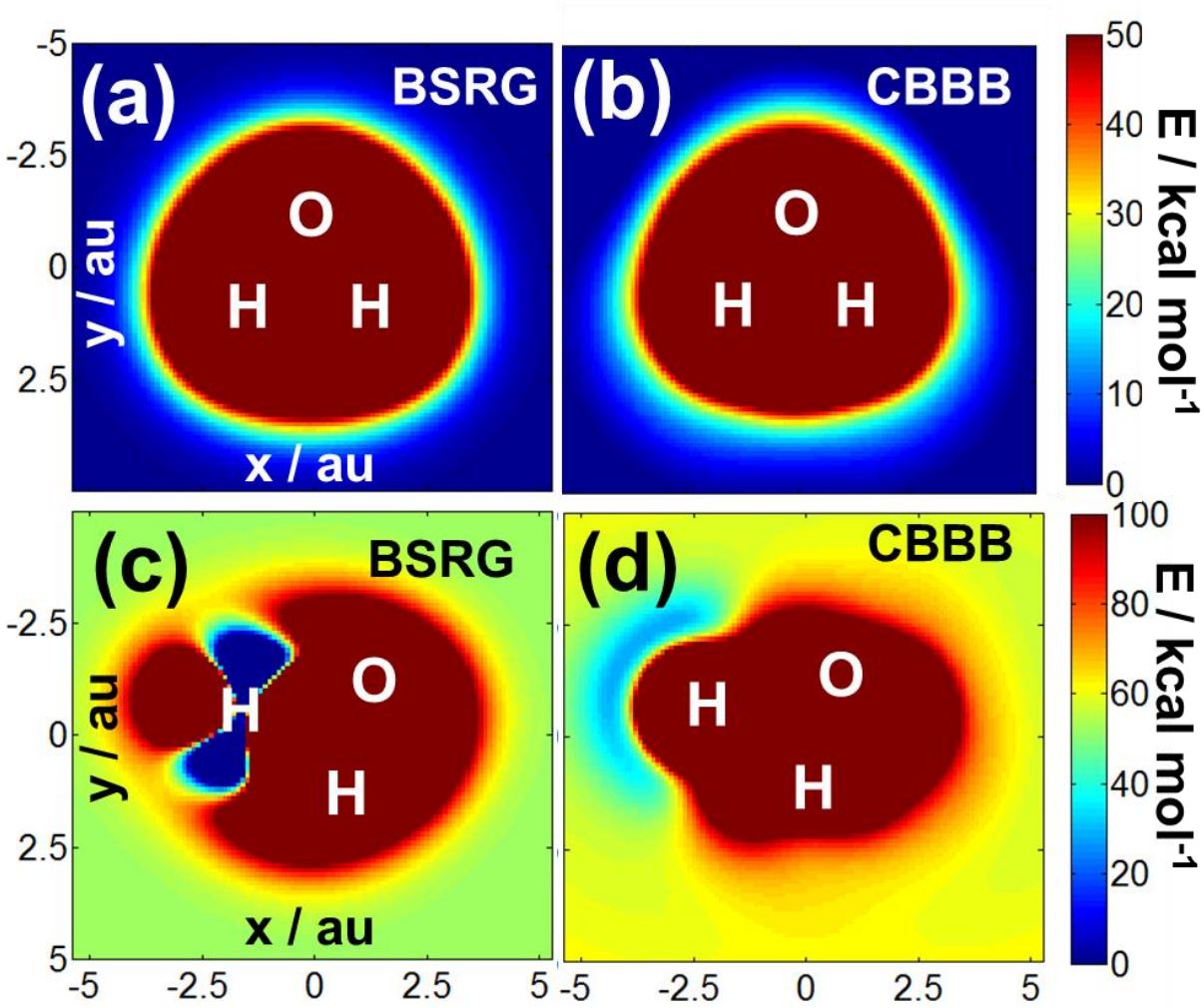

Distribution A: Approved for public release; distribution unlimited.

Figure 2

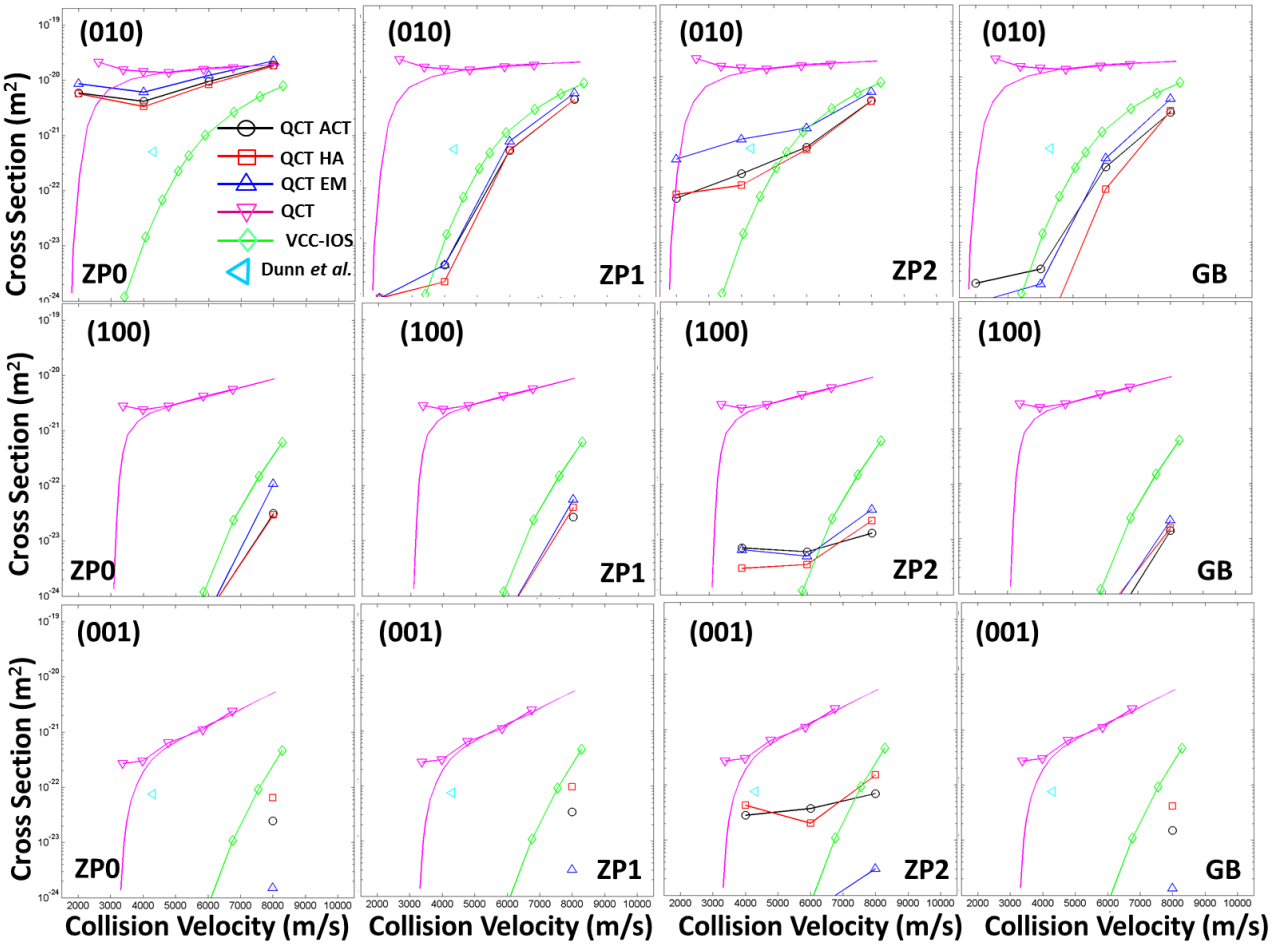

Distribution A: Approved for public release; distribution unlimited.

Figure 3

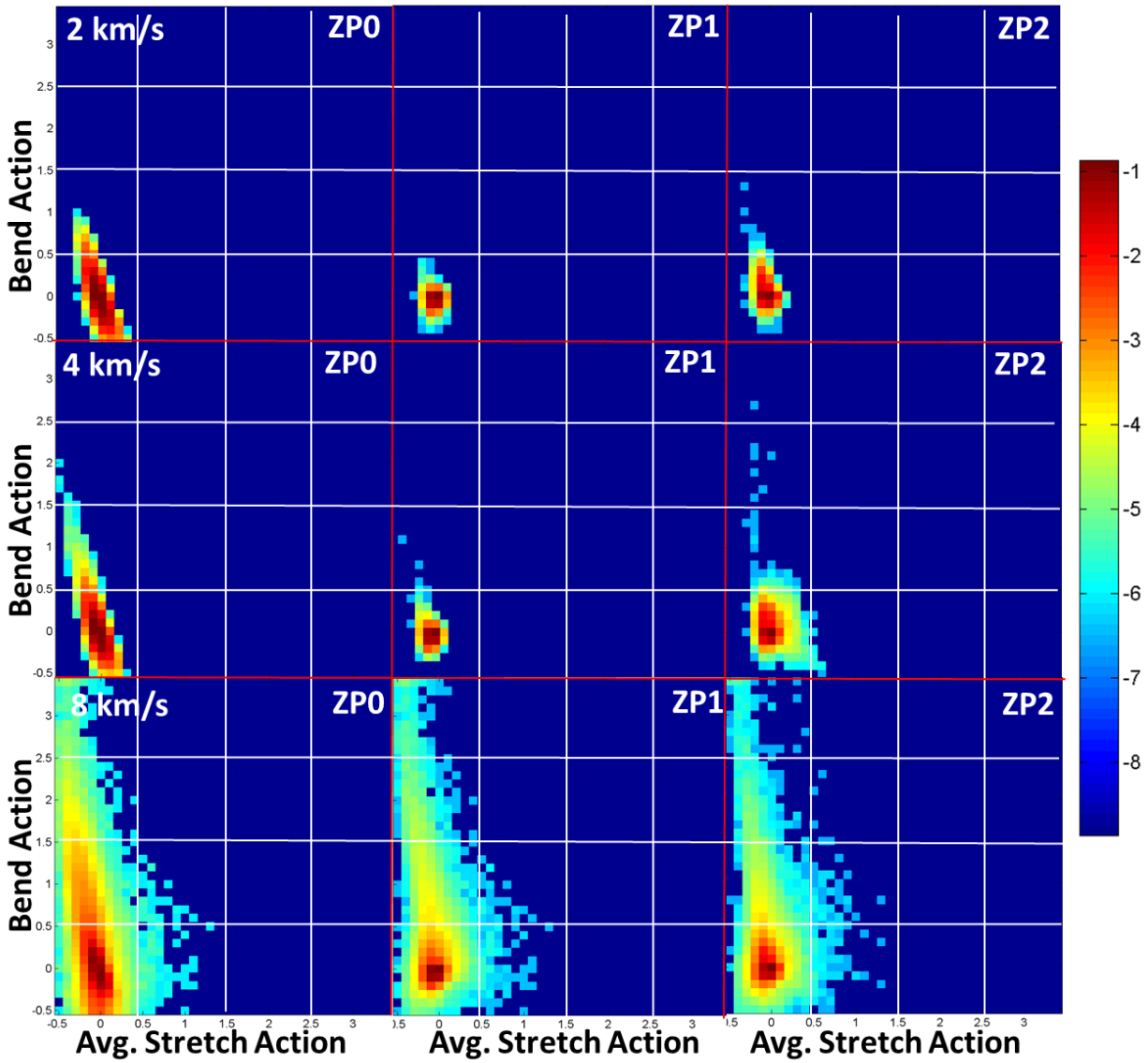

Distribution A: Approved for public release; distribution unlimited.

Figure 4

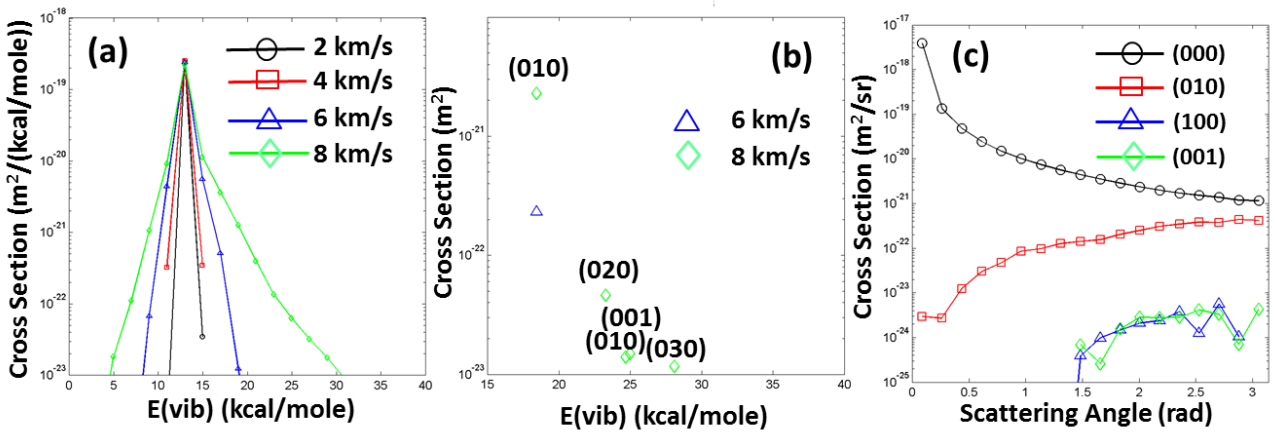

Distribution A: Approved for public release; distribution unlimited.

Figure 5

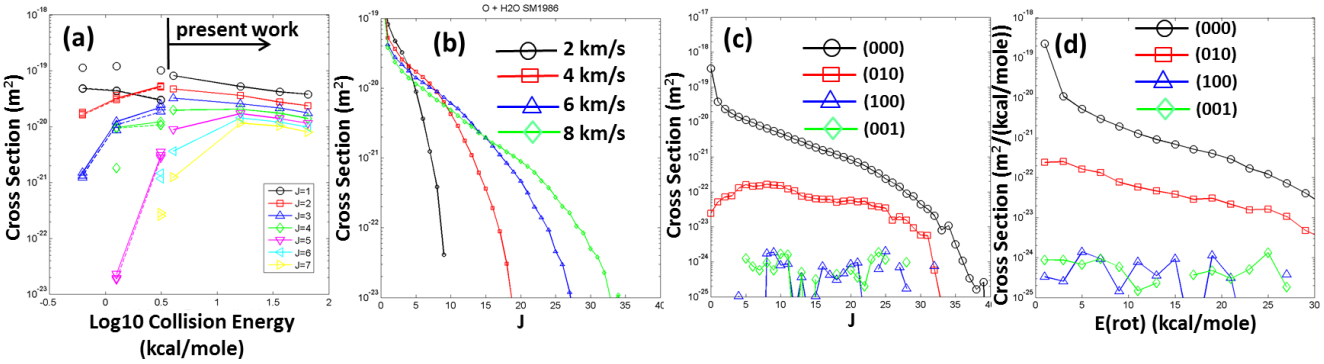

Distribution A: Approved for public release; distribution unlimited.

Figure 6

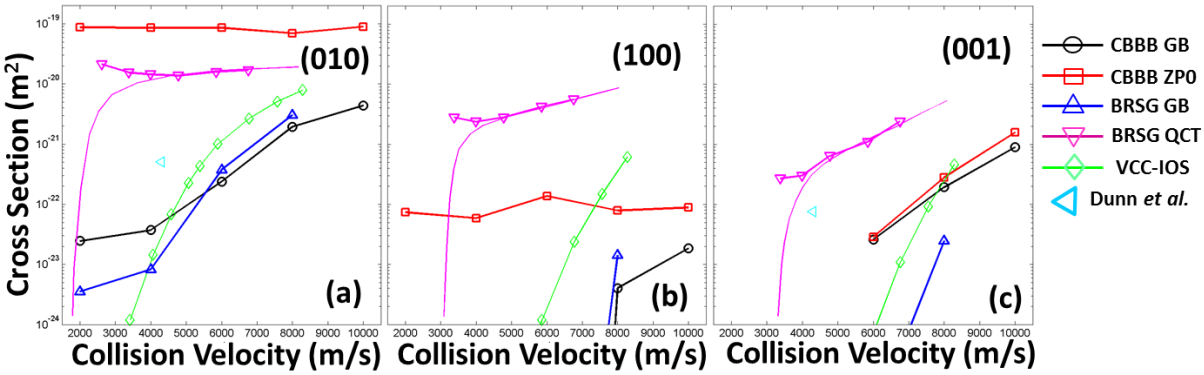

Distribution A: Approved for public release; distribution unlimited.

Figure 7

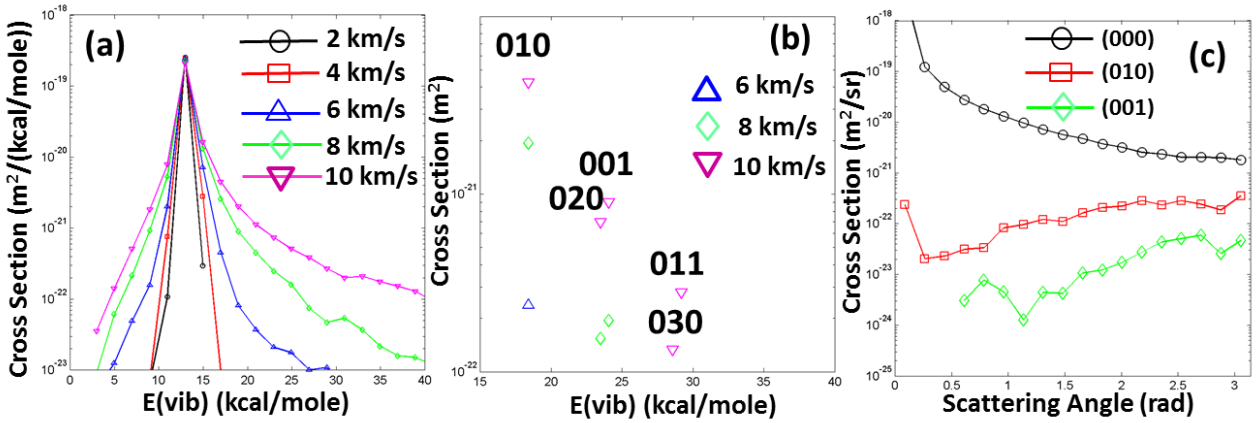

Distribution A: Approved for public release; distribution unlimited.

Figure 8

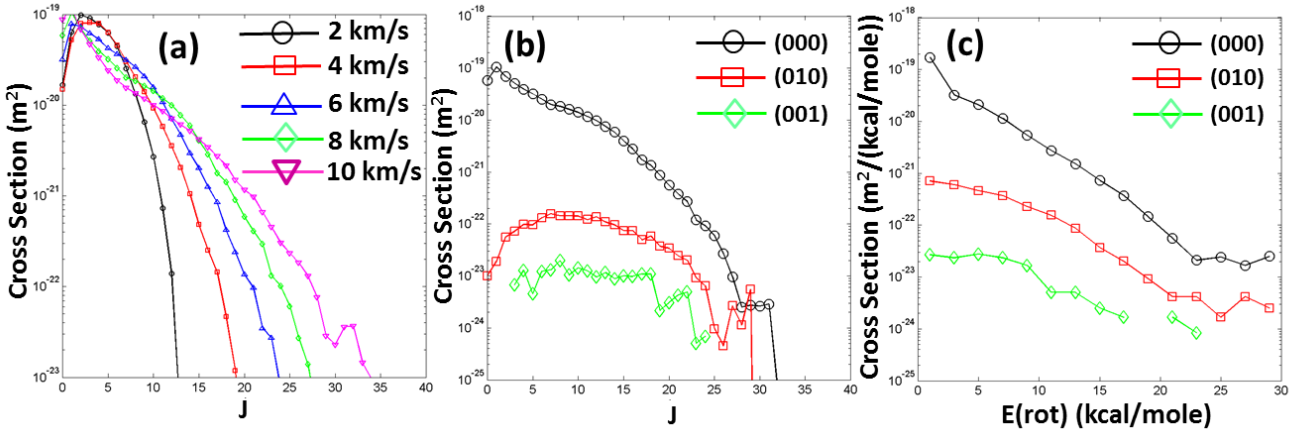

Distribution A: Approved for public release; distribution unlimited.

Figure 9

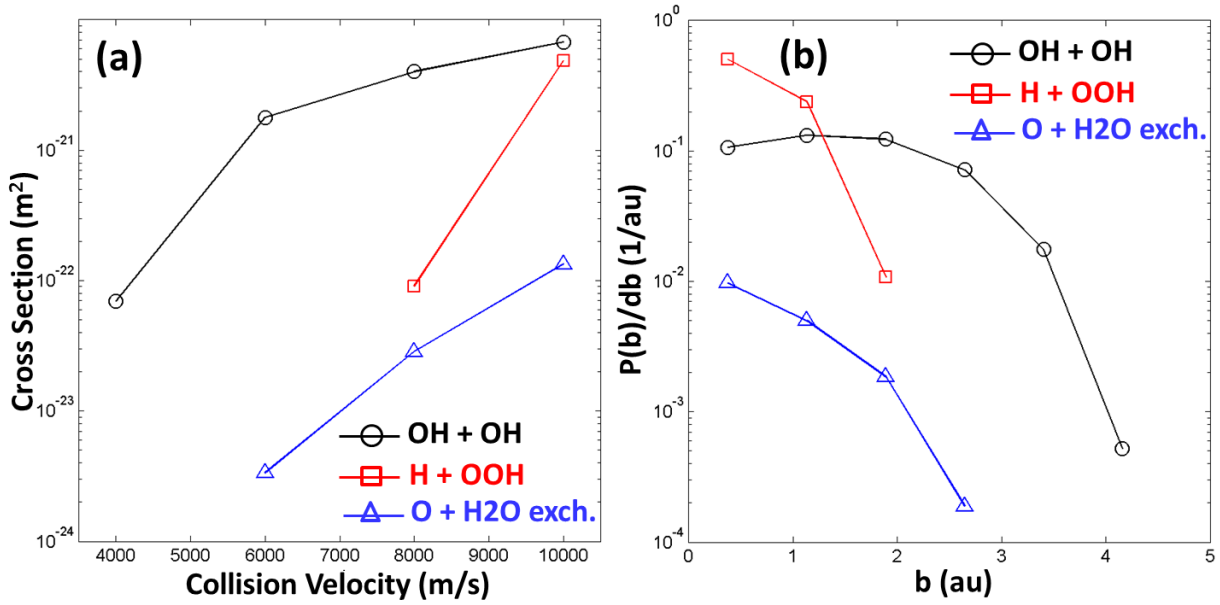

Distribution A: Approved for public release; distribution unlimited.

Figure 10

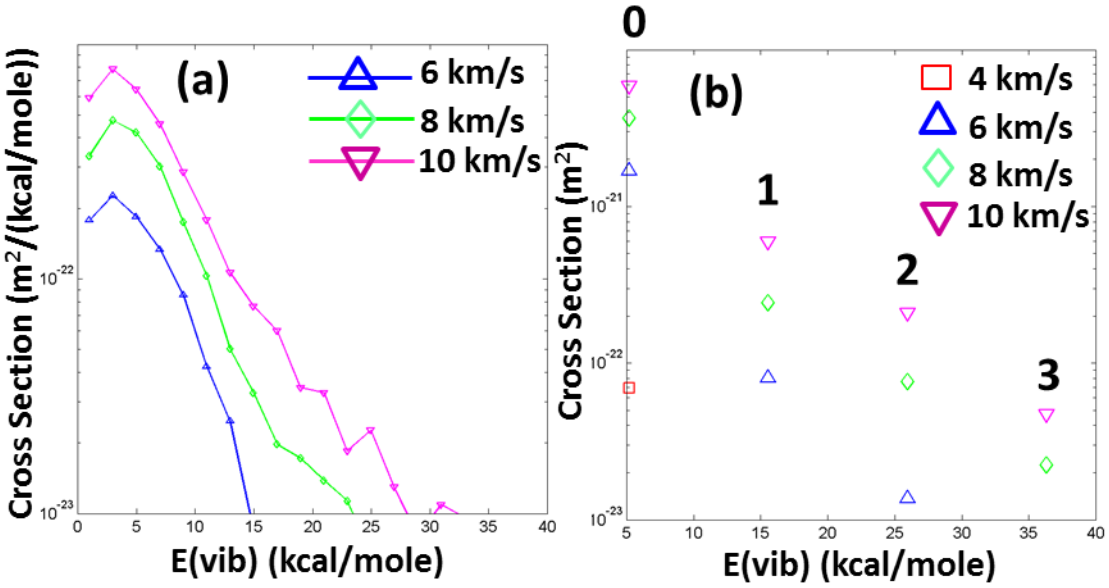

Distribution A: Approved for public release; distribution unlimited.

Figure 11

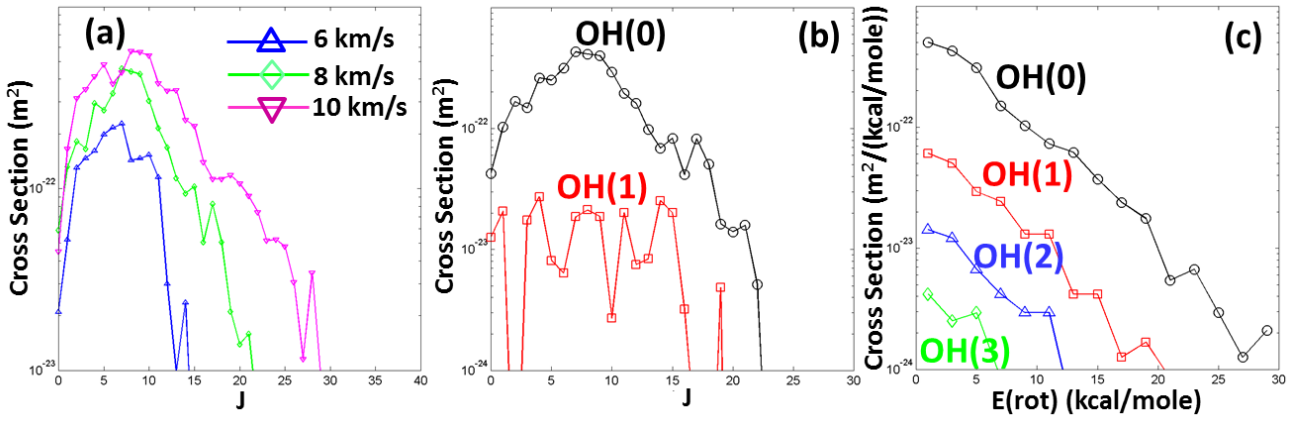

Distribution A: Approved for public release; distribution unlimited.

Figure 12

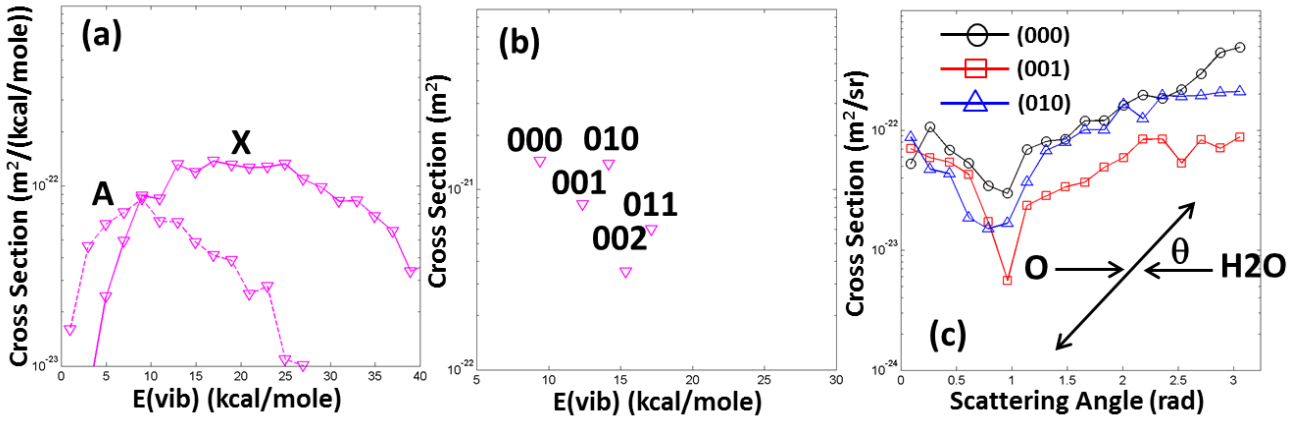

Distribution A: Approved for public release; distribution unlimited.

Figure 13

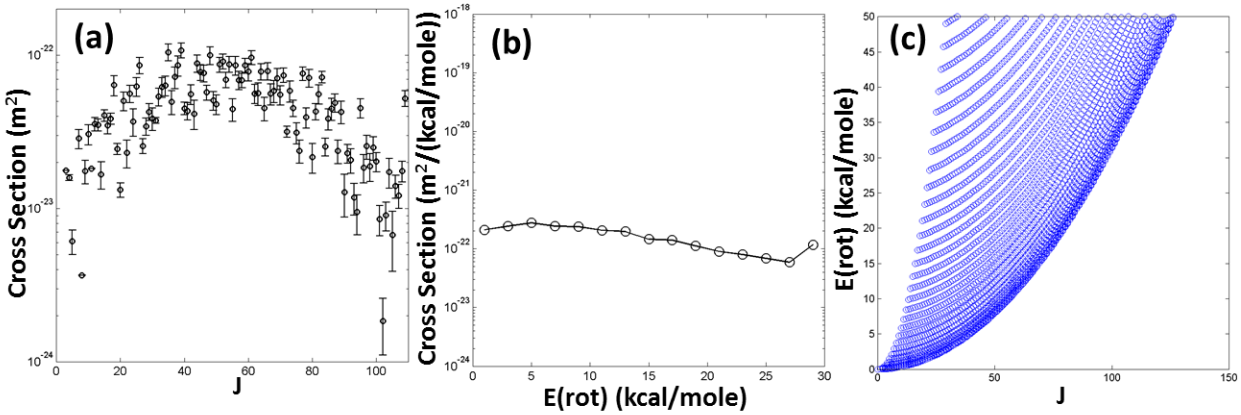

Distribution A: Approved for public release; distribution unlimited.

Figure 14

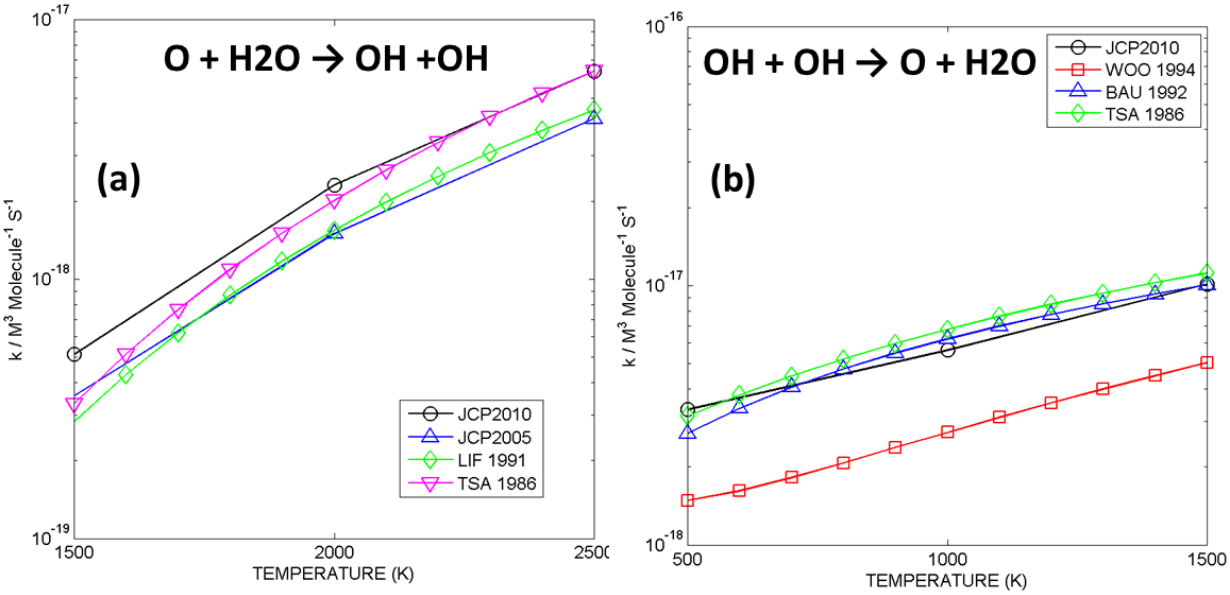

Distribution A: Approved for public release; distribution unlimited.